Information stored in Faraday waves: the origin of a path memory

ANTONIN EDDI[1]†, ERIC SULTAN[2], JULIEN MOUKHTAR[1], EMMANUEL FORT[3], MAURICE ROSSI[4] AND YVES COUDER[1]

[1]Laboratoire Matières et Systèmes Complexes, Université Paris Diderot and CNRS, UMR 7057, Bâtiment Condorcet, 10 rue Alice Domon et Léonie Duquet, 75013 Paris, France

[2]Laboratoire FAST, Université Pierre et Marie Curie, Université Paris-Sud and CNRS, UMR 7608, Bâtiment 502, Campus Universitaire, 91405 Orsay, France

[3]Institut Langevin, ESPCI ParisTech, Université Paris Diderot and CNRS, UMR 7587, 10 rue Vauquelin, 75231 Paris CEDEX 05, France

[4]Institut Jean Le Rond D'Alembert, Université Pierre et Marie Curie and CNRS, UMR 7190, 4 Place Jussieu, 75252 Paris CEDEX 05, France

On a vertically vibrating fluid interface, a droplet can remain bouncing indefinitely. When approaching the Faraday instability onset, the droplet couples to the wave it generates and starts propagating horizontally. The resulting wave–particle association, called a walker, was shown previously to have remarkable dynamical properties, reminiscent of quantum behaviours. In the present article, the nature of a walker's wave field is investigated experimentally, numerically and theoretically. It is shown to result from the superposition of waves emitted by the droplet collisions with the interface. A single impact is studied experimentally and in a fluid mechanics theoretical approach. It is shown that each shock emits a radial travelling wave, leaving behind a localized mode of slowly decaying Faraday standing waves. As it moves, the walker keeps generating waves and the global structure of the wave field results from the linear superposition of the waves generated along the recent trajectory. For rectilinear trajectories, this results in a Fresnel interference pattern of the global wave field. Since the droplet moves due to its interaction with the distorted interface, this means that it is guided by a pilot wave that contains a path memory. Through this wave-mediated memory, the past as well as the environment determines the walker's present motion.

Key words: drops, Faraday waves, pattern formation

1. Introduction

The structure named a *walker* is a recently discovered entity that associates, at macroscopic scale, a particle and a wave (Couder *et al.* 2005*b*; Protière, Boudaoud & Couder 2006). The particle is a droplet bouncing on the free surface of a vertically vibrated fluid layer and the wave is a surface perturbation generated by the droplet impacting the surface. The walker's existence relies on three main factors.

(i) *The possibility of bouncing*. A droplet can be maintained bouncing on a fluid bath if the vibration amplitude is large enough to allow a periodic lift of the droplet (Couder

† Email address for correspondence: antonin.eddi@univ-paris-diderot.fr

et al. 2005*a*). This is observed from acceleration amplitudes comparable to gravity up to the Faraday instability threshold where the interface itself destabilizes (Protière *et al.* 2006).

(ii) *The sustainability of the waves.* As known since Faraday's experiment, forced standing waves appear on the surface of a fluid subjected to a harmonic vertical vibration (Faraday 1831). They form when the oscillating acceleration exceeds a well-defined threshold (Douady & Fauve 1988; Douady 1990). Sustained by parametric forcing, they have a frequency half that of the imposed vibration and their spatial structure usually depends on the container geometry (Ciliberto & Gollub 1984; Keolian *et al.* 1984; Douady 1990). The spatial pattern may also depend on the presence of a multi-frequency forcing (Edwards & Fauve 1994).

(iii) *A coupling between the two processes.* When the forcing amplitude is increased, the bouncing of the drop becomes subharmonically modulated. This is reminiscent of an elastic (Guckenheimer & Holmes 1983) or inelastic (Pieranski 1983) ball on a vibrating plate where periodic, period doubling and chaotic behaviours have been described. In our experiment, there is a range of droplet sizes for which the period doubling becomes complete so that the droplet bounces on the surface only once in two periods. The waves generated by this bouncing have the Faraday frequency and a larger amplitude. Correspondingly, a symmetry breaking occurs: the droplet starts propagating spontaneously on the liquid bath (Couder *et al.* 2005*b*; Protière *et al.* 2006). The walker (the droplet and its associated wave) forms a coherent self-propelled structure.

Two previous experiments investigated the response of the walker when its spread-out wave is split in diffraction experiments (Couder & Fort 2006) or partly transmitted through a barrier (Eddi *et al.* 2009). In both cases, an apparently random response of the droplet was observed in one single realization while it turned out to be statistically deterministic when the experiment was repeated. These results were recovered by a phenomenological model (Couder & Fort 2006) which relies on the superposition of waves generated by the droplet's previous impacts. The resulting *path memory* creates for the walker a specific type of *temporal non-locality*. It has recently been shown that this phenomenon can produce a quantization of possible orbits for a walker subjected to a Coriolis force (Fort *et al.* 2010).

The walker is a steady dissipative structure sustained by the forcing. The transfer of energy to the walker is mediated in two ways, the oscillation of the substrate providing energy to both the wave and the droplet. The system being tuned close to the Faraday instability onset there is a direct parametric forcing of the waves. However, the tuning being below the instability threshold, this direct input is not enough by itself to sustain the waves. The drop also receives kinetic energy, being kicked upwards at each bounce. At its next collision with the surface, the droplet transfers some of its energy to the wave. Altogether, these two energy inputs counterbalance the dissipation and a localized state of Faraday waves is formed. Its size will be shown to be a function of the forcing amplitude.

The present article proposes a more precise characterization of the wave field corresponding to the excitation of a wave in a local region of the bath (the rest of the bath remaining undisturbed). This is a special case of a situation where an extended system exhibits the formation of localized structures. Such structures are known to emerge in different theoretical or experimental contexts. They are usually found in dissipative systems near subcritical bifurcations (see e.g. Fauve 1998; Burke & Knobloch 2006). In such systems, there is a range of values of the control parameter for which two nonlinear stable equilibria can exist. When the system is

spatially extended, the two states can coexist (Thual & Fauve 1988). Most of the space being in one of the states, the localized structures are isolated islands in the other state. It is worth noting that they can interact. When the main focus is to analyse the dynamics of their interaction, they have been described as interacting elementary particles (Aranson 1990). From an experimental viewpoint, localized states are ubiquitous in various physical systems ranging from optics (Ramazza *et al.* 2002) to thermal convection in binary fluid mixtures (Kolodner, Bensimon & Surko 1988), reaction–diffusion systems (Liehr *et al.* 2004) and Faraday instability.

In the Faraday experiment, localized states exist in situations where the onset of the instability is subcritical. They were first observed when the liquid was replaced by a granular medium where localized objects have been called oscillons (Umbanhowar, Melo & Swinney 1996; Tsimring & Aranson 1997). In normal fluids, an hysteresis domain has been found where highly nonlinear propagating solitary states are observed within the linear stable regime (Lioubashevski & Fineberg 2001). This is quite different from the usual Faraday instability and appears when the thickness of the fluid layer is decreased to the order of the boundary layer size. It is due to the highly dissipative character of the flow in this experimental setting (Lioubashevski & Fineberg 2001). However, in the usual Faraday experiment, no localized states are observed below the linear instability threshold since the bifurcation is generally supercritical. For such instabilities, the flow evolution below threshold is simple: once perturbed, the system oscillates but relaxes to its unperturbed base state with a characteristic damping time. The difference in our experiment is that the droplet acts as a local wave exciter.

In this paper, we first describe the experimental set-up (§2) and the observed evolution of the walker wave field with increasing excitation (§3). In §4, we present a phenomenological model of the walker wave field resulting from the superposition of waves emitted. We then measure the formation and decay of the wave resulting from a single impact on the interface (§5), with and without periodic forcing. A fluid mechanical approach (§6) demonstrates how this disturbance can excite, below the Faraday instability threshold, a localized mode of Faraday waves. These results are shown (§7) to provide an understanding of the main characteristics of the wave field of a walker and the path-memory effect.

2. Experimental set-up

Our experiments were performed on the free surface of a fluid contained in a square cell shaken vertically by a vibration exciter (Bruel and Kjaer 4808). A 190 mm × 190 mm cell filled with a liquid layer of depth $h_0 = 4.1$ mm was used, except for the wave field measurements which were performed in a Perspex cell of smaller size (80 mm × 80 mm). The present set of experiments were performed using a silicon oil (Rhodorsyl oil 47V20) of viscosity $\mu = 20 \times 10^{-3}$ Pa s, surface tension $\sigma = 0.0209$ N m^{-1} and density $\rho = 0.965 \times 10^3$ kg m^{-3}. The vibration exciter was sinusoidally driven. The forcing frequency was set to $f_0 = 80$ Hz, which is optimal for the observation of walkers with this oil (Protière *et al.* 2006). An accelerometer measured the amplitude γ of the forcing acceleration.

Figure 1 is a phase diagram showing the different types of bouncing of drops as a function of their diameter D and the forcing amplitude γ/g. In order to obtain drops of a controlled size, we dip a conical pin into the vibrating bath and remove it swiftly (Protière *et al.* 2006). The breaking of the resulting liquid bridge between the bath and the pin generates a single drop. Its size is a simple function of the initial immersion
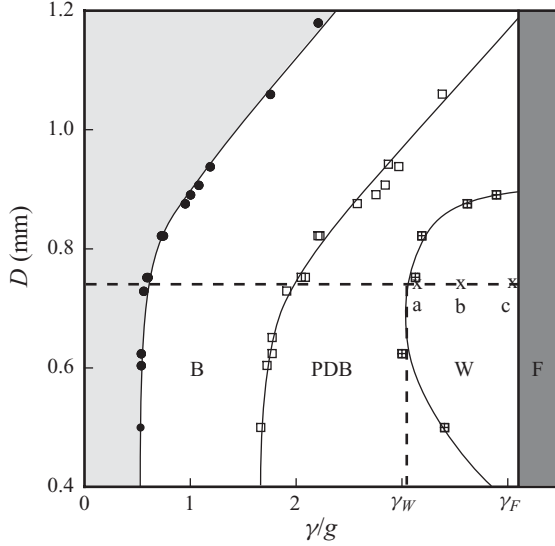
FIGURE 1. Phase diagram of the behaviours of the bouncing droplets as a function of their diameter D and the forcing acceleration γ/g. The fluid is a silicon oil of viscosity $\mu = 20 \times 10^{-3}$ Pa s and the forcing frequency is $f_0 = 80$ Hz. For weak values of γ, the drops do not lift from the surface and coalesce with the substrate (light grey region). In region B, the drops bounce at the forcing frequency on an initially flat interface. In the region marked PDB (for period doubled bouncing), their vertical motion becomes subharmonically modulated. In the region W (for walker), the period doubling is complete and the drops touch the interface only once in two periods. Correspondingly, a drop of a given size becomes propagative when γ exceeds a walking onset γ_W. If the forcing amplitude is increased, the wave field of the walker evolves. The points a, b and c correspond to the three wave fields shown in figure 2. Finally, for larger forcing, the Faraday instability appears at a threshold γ_F. In the dark grey region F (for $\gamma > \gamma_F$), the whole fluid surface is thus covered by Faraday waves. The bouncing of the drop on the corrugated surface becomes chaotic, usually leading to coalescence.

depth of the cone tip. The diameter of the drop is then checked by optical means. This phase diagram is of the same type as that obtained previously by Protière *et al.* (2006), who had used an oil of viscosity $\mu = 50 \times 10^{-3}$ Pa s and a forcing frequency $f_0 = 50$ Hz. For low forcing amplitude, the droplet bounces on a flat interface. As the forcing acceleration is increased, the bouncing becomes subharmonic. For drops having a diameter in the range $650 < D < 820 \, \mu$m, this period doubling becomes complete so that the drop touches the interface once in two periods. This occurs at an acceleration onset $\gamma = \gamma_W$ where the drop couples to the wave, the whole structure becoming a propagative walker. Above a second threshold ($\gamma > \gamma_F$), the fluid surface destabilizes spontaneously and a global pattern of standing waves forms. This is the parametrically forced Faraday instability where the waves have a frequency $f_F = f_0/2$. In our experimental conditions, $\gamma_F = 4.1 \, g$, where g denotes gravity. The measured Faraday wavelength $\lambda_F = 4.75$ mm corresponds to the value computed from the surface wave dispersion relation $\omega(k)$:

$$\omega^2(k) = \left(gk + \frac{\sigma}{\rho} k^3 \right) \tanh(kh_0). \tag{2.1}$$

This relation also provides the wave velocities: their frequency being $f_F = 40$ Hz, their phase velocity is $V_\phi = 189$ mm s^{-1} and group velocity is $V_g = 241$ mm s^{-1}.

The experiments performed in the present work were done using droplets of a typical diameter $D = 760 \pm 10\,\mu\mathrm{m}$. The interesting phenomenology occurs when the system is tuned very close to the Faraday threshold. This requires that in the absence of a drop, the surface of the bath remains undisturbed everywhere. For this purpose, the cell has been carefully manufactured and set perpendicular to the vibration axis. Its fine-tuning was monitored by checking that, at threshold, waves appeared on the whole surface simultaneously.

Several experimental techniques were used (standard and high-speed cameras, correlation techniques) to analyse the motion of the walker and the structure of its wave field. The surface was illuminated from above with a diffuse light gradient. A semi-transparent mirror, set at 45°, was placed between the light source and the fluid bath providing a non-distorted top-view image of the surface.

In order to obtain quantitative measurements of the wave field of the walker we used a recently introduced image correlation technique called the free-surface synthetic schlieren (FS-SS, Moisy, Rabaud & Salsac 2009). This technique, described in detail in this reference, provides an excellent measurement of the instantaneous topography of a disturbed interface. It is based on the comparison of two refracted images of a random dot pattern as observed through the disturbed and undisturbed interface respectively. Using a digital image correlation (DIC) algorithm, the displacement field between these two images is obtained. It can be shown (Moisy *et al.* 2009) that to first order in paraxial angles, in surface slopes and in relative deformations, the surface gradient is simply proportional to the displacement field. This gradient field is then integrated to obtain a reconstruction of the surface height of the interface. This is done by a least-square inversion of the gradient operator.

In practice, we use a specifically designed cell, the bottom of which is a thick Perspex plate. A white screen covered with randomly disposed black dots is glued under this plate. It is photographed from a large distance (1.3 m) to minimize the paraxial effects. The optical distance between the interface and the dotted screen is the sum of the optical thickness of the oil and Perspex layers, their refractive indices being similar. This distance between the interface and the screen is chosen to obtain an optimum strain of the refracted image. It has to be as large as possible to increase the resolution, but still to remain smaller than the critical distance for which caustics would appear. It has thus to be chosen as a function of the observed surface slopes. With typically five dots per square millimetre and a distance between the interface and the screen of 25 mm we thus obtain the shape of the wavepacket of the walker on a typical area $45\,\mathrm{mm} \times 45\,\mathrm{mm}$ (1000×1000 pixels) with a resolution of $0.5\,\mu\mathrm{m}$ vertically and 0.3 mm horizontally.

3. Characterization of a walker

At each bounce, the droplet hits a surface distorted by the waves produced at previous impacts. Protière *et al.* (2006) have shown that the vertical bouncing of a droplet becomes unstable when the amplitude of the wave on which it bounces becomes large enough. A symmetry-breaking bifurcation then arises: the droplet becomes spontaneously propagative on the bath surface with a mean horizontal velocity V_W (Couder *et al.* 2005b). In practice, when the forcing amplitude increases, the bouncing becomes subharmonic but the period doubling is not complete. In a finite range of droplet sizes ($0.720 < D < 0.820$ mm), this period doubling becomes complete: the droplet impacts the interface once in two vibration cycles. The amplitude of the waves then increases abruptly since the droplet becomes a source of waves at

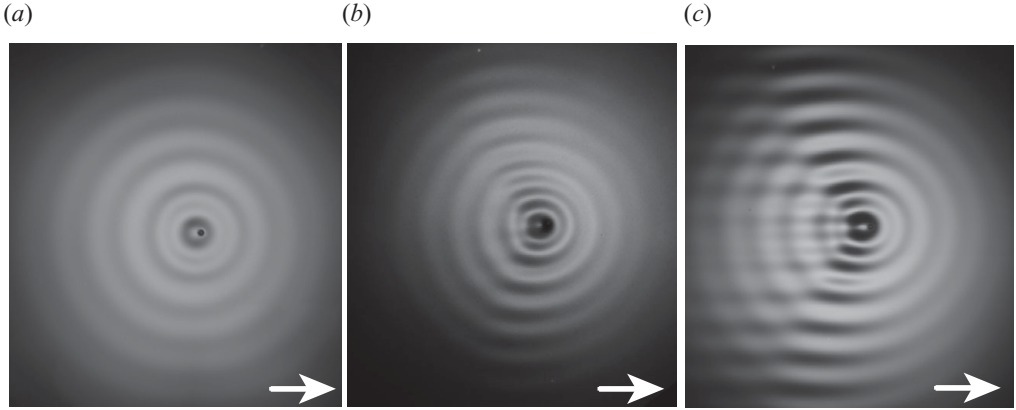(*a*)   (*b*)   (*c*)

FIGURE 2. Photographs of the wave field associated with the same droplet of diameter $D = 0.76$ mm for three different forcing accelerations in the walking regime (points a, b and c of the phase diagram, see figure 1). The drop propagates from left to right. (*a*) Wave field observed at point a, where $\Gamma = (\gamma_F - \gamma)/\gamma_F = 0.17$, i.e. $\Gamma^{-1} = 5.9$. (*b*) Wave field at b, where $\Gamma = 0.07$, i.e. $\Gamma^{-1} = 14.3$. (*c*) Wave field at c, where $\Gamma = 0.018$, i.e. $\Gamma^{-1} = 55.5$. The value of Γ^{-1} gives an order of magnitude of the number of bounces which contribute to the wave field interference pattern.

the Faraday frequency. This complete period doubling occurs when the acceleration exceeds a well-defined acceleration γ_W which depends on D. The droplet moves spontaneously on the bath in the whole complete subharmonic bouncing regime, $\gamma_W < \gamma < \gamma_F$, with a velocity V_W which increases with γ. Note that for smaller droplets, the bouncing dynamics is more complex, and the trajectory is not rectilinear ($0.650 < D < 0.720$ mm).

In the walking regime, the wave pattern created by the walker evolves when the forcing acceleration γ increases. Figure 2(*a–c*) displays photographs of the wave field of the same walker with a rectilinear trajectory for three different values of γ, getting closer to γ_F. To avoid finite size effects, experiments were performed far away from the cell boundaries. The aspect of the wave field is controlled by the non-dimensional distance $\Gamma = (\gamma_F - \gamma)/\gamma_F$ to the Faraday threshold. Immediately above the walking threshold ($\Gamma = 0.17$, in figure 2*a*), the wave field remains approximately circular with a slight Doppler shift. For larger forcing ($\Gamma = 0.07$, in figure 2*b*), it develops a horseshoe aspect. Finally, for a forcing close to γ_F ($\Gamma = 0.018$, in figure 2*c*), waves extend further away, have a larger amplitude and a long lasting and complex interference pattern appears behind the droplet.

As discussed in Fort *et al.* (2010) and below, this structure results from the interferences of waves that keep surrounding the previously visited points. Because of the proximity of the Faraday threshold, these waves are almost sustained and kept synchronous by the forcing. The observed interference structure (see §7.3) contains information about the walker's recent trajectory. This is a path memory that will be determinant since the droplet's motion is generated by the wave structure.

In the following (§5), using single disturbances, we measure, for $\gamma < \gamma_F$, the non-dimensional damping time τ/T_F of the Faraday waves. In the case of repeated collisions it is a measure of the number of past collisions that keep contributing to the wave field. For this reason we call the dimensionless number $Me = \tau/T_F$, the memory parameter. We are in the vicinity of a supercritical bifurcation which is described by a Mathieu equation. It is shown in §6.1 why the relaxation time of a

disturbance is expected to be proportional to Γ^{-1} the inverse of the distance to the instability onset. In the single impact experiments, we found that the proportionality coefficient is approximately equal to 1. For this reason, Γ^{-1} can be used as an approximation of Me in the walker's situations where the measurement of τ/T_F cannot be done directly. In this approximation, the wave fields exhibited in figure 2(*a–c*) correspond to increasing values of the memory parameter $\Gamma^{-1} = 6$, 14 and 55, respectively. The finite size of the bath does not allow the possibility of getting nearer to the Faraday instability threshold: when γ reaches γ_F, Me diverges. In this situation, the waves generated by the drop are no longer damped: they reflect on the cell's boundaries and finally form a standing wave pattern in the whole cell. The wave field is now defined by the cell geometry and the droplet is no longer its source. The lock-in phenomenon is then lost and the bouncing becomes temporally chaotic, usually leading to the coalescence of the droplet with the bath.

In order to get a quantitative measurement of the wave fields, we used the above-described image correlation technique (Moisy *et al.* 2009). The comparison of two experimental fields obtained with a droplet of diameter $D = 760\,\mu$m is presented in figure 3(*a,b*) for two forcing accelerations corresponding to $\Gamma^{-1} \simeq 5$ and $\Gamma^{-1} \simeq 17$, respectively. In the former, the wave is approximately isotropic while, in the latter, an anisotropy appears. The relative positions of nodes and antinodes of the structure are better observed in figure 4(*a*), which is a surface map corresponding to the same wave field as figure 3(*b*). Along the direction of propagation, we observe the horseshoe structure, the waves of largest amplitude being emitted in two well-defined lateral lobes. The horseshoe is limited behind the drop by a line of destructive interference (see § 7.3). Behind this line, the wave field exhibits a pattern of nodes and antinodes, distributed symmetrically on each side of the walker's past trajectory.

We can also examine the evolution of the walker velocity V_W as a function of γ for a droplet of diameter $D = 790\,\mu$m (see figure 4b). Near the onset, velocity V_W grows as the square root of the distance to threshold, i.e. $V_W \propto (\gamma - \gamma_W)^{1/2}$. This has already been observed and documented by Protière *et al.* (2006). In that article, a simple model showed that the interaction of the bouncing droplet with waves of increasing amplitude leads to a pitchfork bifurcation at which the motionless droplet becomes propagative. The control parameter is proportional to the amplitude of forcing while the order parameter is the mean horizontal velocity V_W. The square root dependence was thus predicted and experimentally checked. As shown in figure 4(*b*), for accelerations larger than $\gamma = 3.8\,$g the velocity saturates and remains constant at a value $V_W^{max} = 11.5\,$mm s^{-1}. This is an effect of the superposition of waves along the axis of propagation. In the bouncing region, the contribution to the slope of the older sources is cancelled out by destructive interference, so that they do not contribute to the forward motion.

4. Phenomenological model and its results for the walking regime

4.1. *Phenomenological model*

To understand the dynamical properties of walkers, a phenomenological approach was developed. It relies on a simple modelling of the coupling between the droplet and the fluid surface. The wave characteristics are imposed without being connected to the full fluid dynamics description. In spite of its simplifying assumptions, this model led to simulations where the diffraction of walkers (Couder & Fort 2006) or their orbital motion in a rotating system (Fort *et al.* 2010) have been reproduced
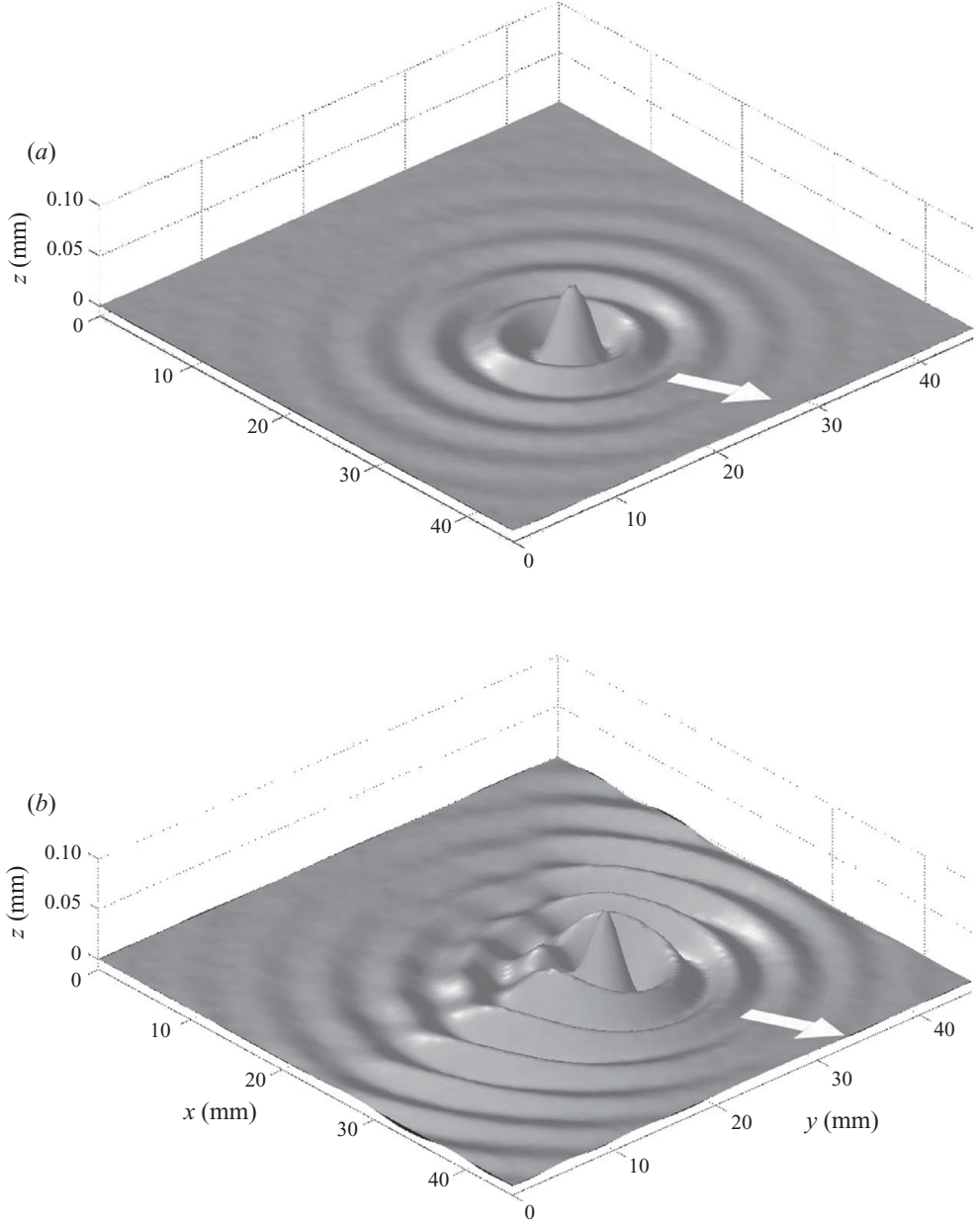
FIGURE 3. Measured wave fields of walkers (a droplet of diameter $D = 760\,\mu\text{m}$) for two forcing accelerations. The walkers move in the direction given by the arrows. (a) $\gamma = 3.25\,g$ ($\Gamma^{-1} = 4.8$): the wave pattern around the walker remains close to circular and the droplet moves at $V_W = 7.53 \pm 0.05\,\text{mm}\,\text{s}^{-1}$. (b) $\gamma = 3.75\,g$ ($\Gamma^{-1} = 17.2$): the associated waves are more intense and take a horseshoe aspect, and interferences are visible in the wake behind the droplet, which moves at $V_W = 11.05 \pm 0.05\,\text{mm}\,\text{s}^{-1}$.

with a good accuracy. In §6, we a develop a theoretical model. This fluid mechanical approach will identify the exact wave characteristics.

The motion of the droplet is computed iteratively bounce after bounce. It is first assumed that the vertical motion of the droplet is decoupled from its horizontal
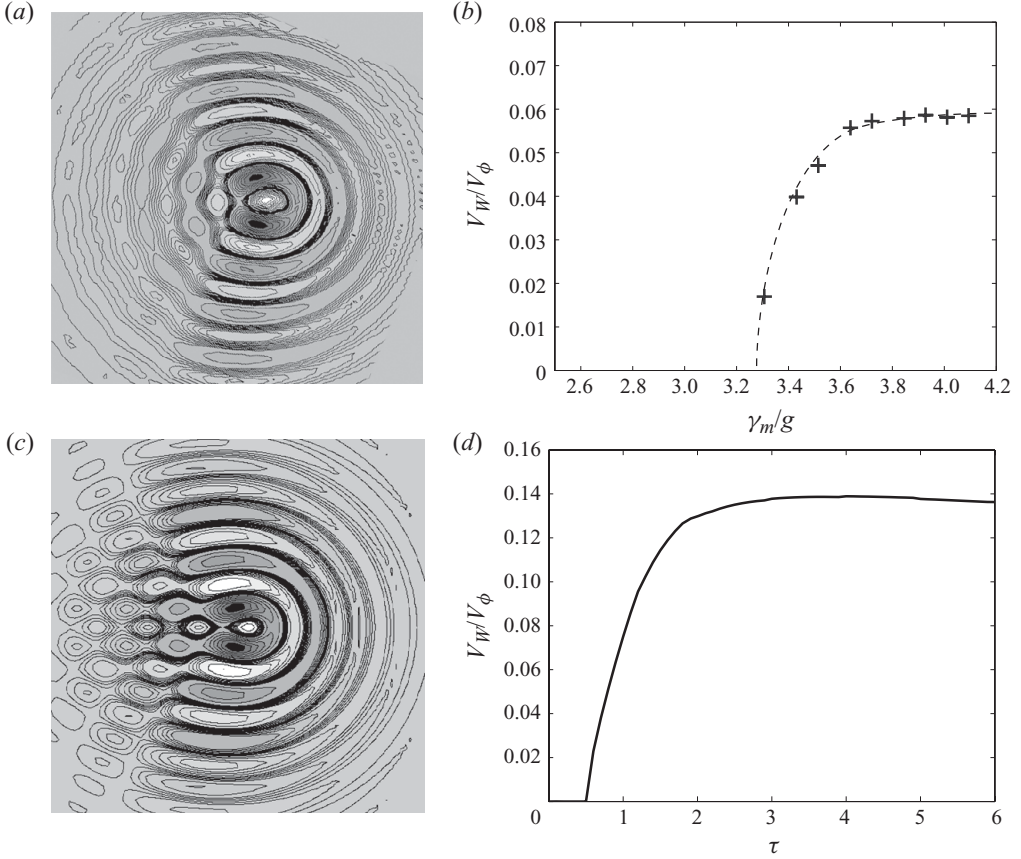
(a)

(b)

(c)

(d)

FIGURE 4. (a) Experimental measurement of the wave field with a walker of diameter $D = 760\,\mu\text{m}$ moving at $V_W = 11.05 \pm 0.05\,\text{mm s}^{-1}$, with $(\Gamma^{-1} = 17.2)$. (b) Non-dimensional experimental velocity V_W/V_ϕ of a walker as a function of non-dimensional acceleration γ/g. Experiment with a droplet of diameter $D = 790\,\mu\text{m}$ and an oil of viscosity $\mu = 20 \times 10^{-3}\,\text{Pa s}$. Dots are experimental values and the dashed line is an interpolation. (c) Wave field obtained by numerical simulation ($\delta/\lambda_F = 1.6$, $Me = 30$, $A/\lambda_F = 5 \times 10^{-2}$, $0.4\tau_F$). (d) Non-dimensional velocity V_W/V_ϕ in a numerical simulation of the model as a function of the characteristic memory time τ.

motion and that the take-off and landing times are determined by the vertical oscillation of the liquid bath as if the collision was inelastic. For a range of forcing accelerations, the vertical motion is periodic of period $T_F = 1/f_F$. At each take-off, the droplet is given a vertical velocity equal to the surface velocity.

The droplet horizontal velocity is computed separately at each bounce. It is given by adding two terms to the velocity before the bounce.

(i) A factor that models the viscous damping due to the shearing of the air film separating the drop from the bath.

(ii) An increment of speed due to the impact on a slanted surface. This kick is proportional to the local slope of the surface: it is zero if the surface is horizontal.

After its take-off, the droplet retains a constant horizontal velocity and has a free parabolic motion. The velocity at take-off determines the elementary horizontal displacement $\delta \boldsymbol{r}_n$ during the free flight of the droplet and thus the landing point.

The core of the computation is in the calculation of the interface slope at the point of landing. More generally, one wants to compute the whole topography of the wave

field, i.e. the height $\xi(\boldsymbol{r}, t_i)$ of the interface at point $\boldsymbol{r}$ and time t_i. Here one assumes that it results from the linear superposition of in-phase waves originated at previous impact points. To compute the slope under the droplet, we need to give an explicit expression for the wave emitted at each bounce. Our model uses circular waves at the Faraday frequency and centred at the points $\boldsymbol{r}_n$ where the droplet has previously impacted on the interface. Taking into account the vertical forcing and the resulting memory effect, we add up the contributions of the previous bounces and compute the surface height:

$$\xi(\boldsymbol{r}, t_i) = \sum_{n=-\infty}^{i-1} \mathrm{Re}\left[\frac{A}{|\boldsymbol{r} - \boldsymbol{r}_n|^{1/2}} \exp\left(-\frac{t_i - t_n}{\tau}\right) \exp\left(-\frac{|\boldsymbol{r} - \boldsymbol{r}_n|}{\delta}\right) \exp\left(\mathrm{i}\frac{2\pi|\boldsymbol{r} - \boldsymbol{r}_n|}{\lambda_F} + \phi\right)\right],$$
$$(4.1)$$

where Re denotes the real part, A stands for the wave amplitude at each impact and $\boldsymbol{r}_n$ stands for the positions of the previous impacts at times $t_n = t_i - (i - n)T_F$ with $n < i$. We use a sinusoidal dependence to account for the spatial oscillation. It is necessary for the accuracy of these simulations to introduce two independent damping factors. The localized nature of the wave field was introduced in the simulations by an algebraic decay that accounts for the wave radial propagation and an exponential spatial damping. This spatial decay, due to the viscous dissipation of the front of the disturbance, is characterized by the length scale δ. The temporal decay time concerns the Faraday standing waves triggered by this disturbance. Since the system is tuned below but close to the Faraday instability threshold, each elementary wave is almost sustained: its amplitude declines with a typical decay time τ. In this model, the non-dimensional damping time is the memory parameter $Me = \tau/T_F$. It is tunable, being determined by the distance to the Faraday instability threshold. The origin of these two dampings will be detailed in § 5.

4.2. *Walking regime*

A first verification of the model is to obtain the walking bifurcation. In the experiment, the control parameter is simply γ. In the model, several free parameters (A, δ, τ) are related to γ but their dependences are not simple. In order to study the walking onset, we assume that the walker has a very small horizontal velocity (about $10^{-4}V_\phi$), and we compute the time evolution of its horizontal position for 5000 bouncing cycles. For weak values of the wave amplitude A or large damping τ^{-1}, the droplet stops and remains motionless. Increasing A or decreasing τ^{-1} leads to the walking transition. This walking bifurcation is analogous to the pitchfork bifurcation experimentally observed (Protière *et al.* 2006).

Experimentally, the velocity V_W saturates when the memory effect increases. For this reason, we performed a series of simulations changing the memory parameter τ. Figure 4(*d*) is a plot of the non-dimensional asymptotic velocity V_W/V_ϕ as a function of the memory parameter τ. If the characteristic damping time τ is larger than a threshold value $\tau_W = 0.53$, the droplet starts moving. Its velocity increases with τ and saturates to a value about $V_W^{max} = 0.14\, V_\phi$. Such large asymptotic velocities correspond to the case of large droplets in the experiment. In the numerical simulations, the value of V_W^{max} depends on the chosen amplitude A. The wave fields produced by these simulations reproduce quite accurately the experimental observations, as can be seen by a comparison of figure 4(*c*) with figure 4(*a*).

Since the phenomenological model is based on a superposition of waves emitted at each bounce, we were led to analyse experimentally and theoretically the wave structure emitted by one bounce when γ approaches the Faraday instability threshold γ_F.
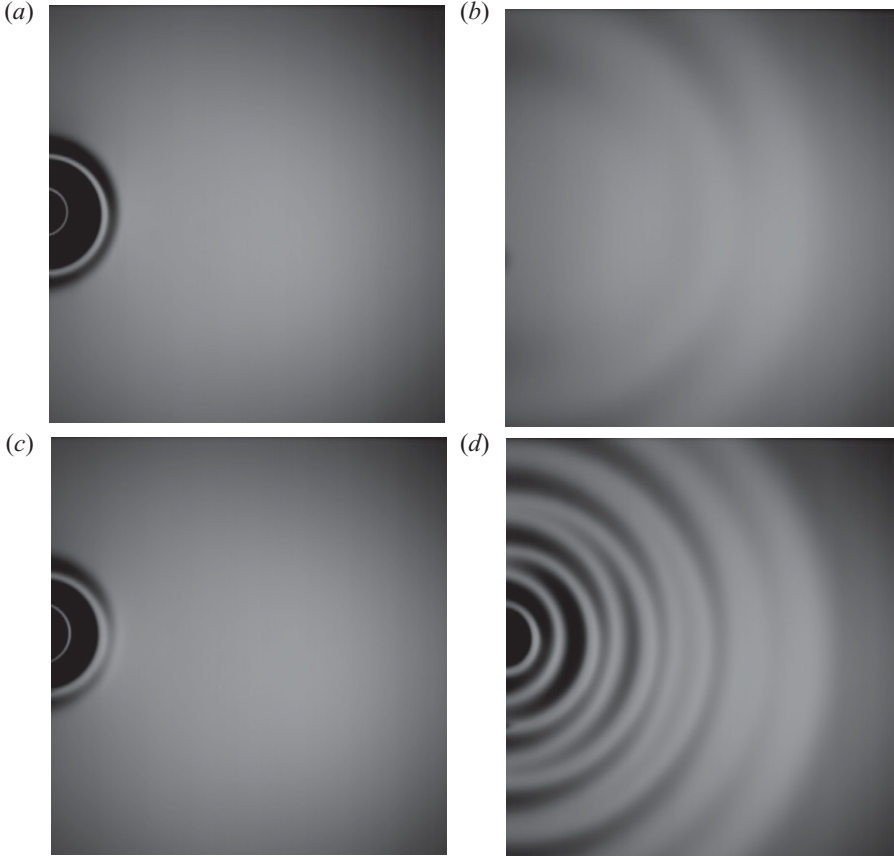
(a)

(b)

(c)

(d)

FIGURE 5. Photographs of the wave field generated on the bath by the fall of a steel ball of diameter $d = 2$ mm. Pictures are taken at times $t_1 = 51$ ms (*a,c*) and $t_2 = 173$ ms (*b,d*) after the collision. In (*a*) and (*b*), the bath is not vertically oscillated. In (*c*) and (*d*), the vertical acceleration is very close to the Faraday instability onset $\Gamma \simeq 0.01$ or ($\Gamma^{-1} = 100$).

5. Experimental wave field generated by a single impact

In the set of experiments presented in this section, a steel ball (of size comparable to the droplet) was dropped into the bath where it immediately sank. It thus disturbed the interface by only one single impact. The assumption is that the localized hollow generated at short times is larger but somewhat similar to the localized hollow created by a single bounce of a droplet. Figure 5 shows the general aspect of the resulting waves at times $t = 51$ ms and $t = 173$ ms in the absence (figure 5*a,b*) or in the presence (figure 5*c,d*) of forcing vibration. As shown in figure 5(*a,c*), the initial disturbance is the same, but in the absence of forcing, the splash generates only a radially propagating wavepacket similar to that of a stone thrown in a pond. In the presence of forcing ($\Gamma^{-1} = 100$), a similar propagating wavepacket is initially generated but, behind this wavepacket, the interface does not immediately return to rest. Standing waves of wavelength $\lambda_F = 4.75$ mm are observed to continue oscillating and finally slowly decay (figure 5*d*).

Measurements of the spatio-temporal evolution of these waves can be done using the digital image correlation technique. Figure 6 displays three-dimensional (3D) plots of the temporal evolution of a radial cross-section of the interface for three different γ,
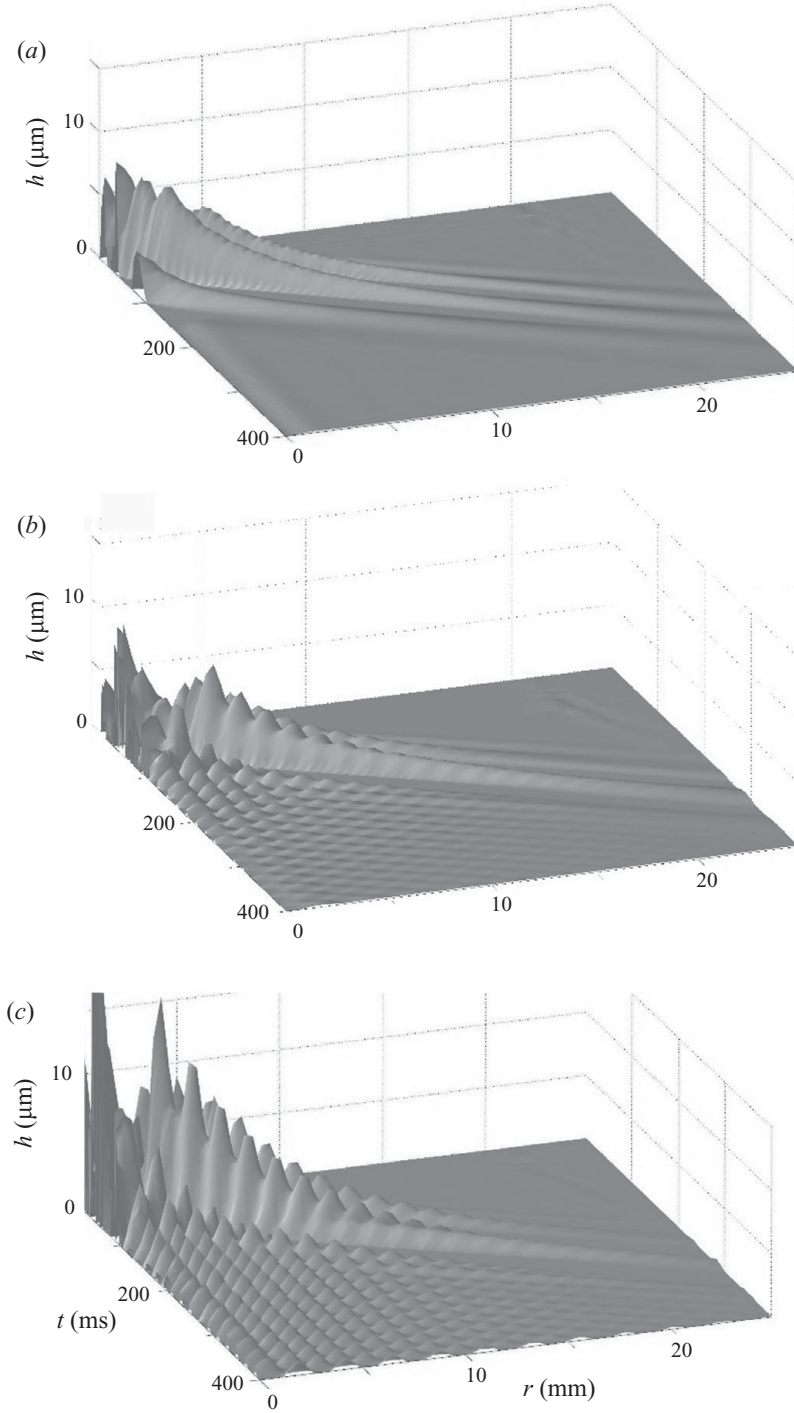
FIGURE 6. Spatio-temporal 3D reconstruction of the wave propagation away from the point of impact of a steel ball on the bath (at time $t = 0$). The liquid height is measured with an accuracy of 5×10^{-4} mm. The bath is subjected to vertical accelerations such that (a) ($\Gamma^{-1} = 1.25$), (b) ($\Gamma^{-1} = 5$) and (c) ($\Gamma^{-1} = 32$). In all three cases, the radial propagation of a similar wavepacket is observed. In the presence of oscillations, sustained Faraday waves are triggered by this disturbance. Their amplitude and temporal extent increase as *Me* increases.
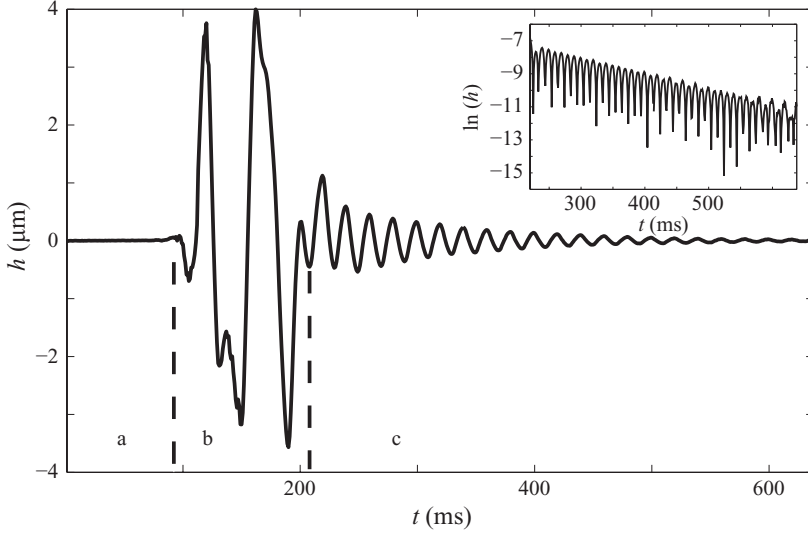
FIGURE 7. The temporal evolution of the liquid height at a point located 5.3 mm away from the ball impact. The bath is subjected to a non-dimensional acceleration $\Gamma = 0.2$. It takes 95 ms for the disturbance to reach the point of measurement (region a). In region (b), the propagating capillary wave passes the measurement point. A Faraday wave then survives, damped on a typical time τ. The inset shows a log-linear plot of the amplitude of the wave in region (c), confirming an exponential decay with $\tau = 110$ ms. The measured non-dimensional damping time $\tau/T_F = 6.25$ is the real value of the memory parameter. It is close to the expected value $\Gamma^{-1} = 5$.

increasingly close to γ_F. These measurements confirm the coexistence of two types of waves. The initial disturbance always generates a wavepacket of travelling waves that propagate away. The mean wavelength observed in this wavepacket is related to the ball size. With a ball of diameter $D = 2$ mm, the mean wavelength is a few times the capillary scale of order $\lambda_{capil} \simeq 1.5$ mm. When the forcing is large enough (figure 6b,c), the fluid, after the wavepacket has passed, keeps oscillating and a stationary wave pattern remains which decays slowly. It oscillates at frequency f_F and has Faraday wavelength λ_F.

The spatial and temporal decay of the oscillation can be obtained from these measurements independently. We can first measure the spatial decrease of the capillary waves wavepacket away from the point of impact. In a non-dissipative situation, this amplitude should only decrease because of its radial propagation. In reality, the measured spatial decrease exhibits an exponential decay due to the added effect of viscous dissipation. We checked that this spatial decay rate depends on the fluid used for the experiment. In our experimental conditions, we find a typical damping distance $\delta = 1.6\lambda_F$.

The temporal decay of the oscillation can be investigated independently by a measurement of the surface disturbance at a fixed point as a function of time. Figure 7 presents the temporal evolution of the liquid height at a location situated 5.3 mm away from the ball impact. This corresponds to the case shown in figure 6(b), the bath being subjected to a non-dimensional distance to Faraday threshold $\Gamma = 0.20$. It takes 95 ms for the disturbance to reach the point of measurement (region a in figure 7). In region (b), the propagating capillary wave passes the measurement point disturbing the interface. A slowly decaying Faraday wave then survives in region (c).

The log-linear plot in the inset (figure 7) shows the exponential decay of the amplitude in region (c). The measured temporal decay rate, $Me = \tau/T_F = 6.25 \pm 0.5$, is the real memory parameter Me. Its value is close to that expected from the distance to the Faraday threshold $\Gamma^{-1} = 5$. When the same measurement is done in the case shown in figure 6(c), where $\Gamma = 0.032$, we find $Me = \tau/T_F = 25 \pm 5$, a value close to $\Gamma^{-1} = 31$. More generally, for all the cases measured, we found the value of the non-dimensional decay time τ/T_F to be close to Γ^{-1}. This could be expected: it corresponds to what is observed in systems that are unstable by a supercritical bifurcation scenario. When disturbed immediately below their instability threshold, these systems respond by an oscillating behaviour that is damped with a damping time τ/T_F inversely proportional to the distance to threshold. At threshold, the decay time diverges and the oscillation is sustained. Here, the control parameter being the non-dimensional acceleration, the expected damping time is $\tau/T_F \propto ((\gamma_F - \gamma)/\gamma_F)^{-1}$. A more complete analysis given in § 6.1 confirms this result.

Finally, it can be noted that at each point of the surface, the initial amplitude of the Faraday oscillation is determined by the amplitude of the capillary wave that reaches this point and triggers these oscillations. This observation justifies the necessity of introducing both a decay length and a decay time in the phenomenological model (4.1).

6. Single impact on a vibrating bath: a fluid mechanics point of view

In this section, we propose a simple fluid mechanical model that contains the main building blocks of the wave dynamics presented in the experimental sections. We consider an incompressible liquid of depth h_0 contained in a tank vertically located at $z = z_0 \cos(\omega_0 t)$. The horizontal size of the tank is assumed large compared with the size of the localized structure. This corresponds to the experimental situation and ensures that the tank boundaries do not play a role. The tank undergoes an acceleration in the vertical direction of $-\gamma \cos(\omega_0 t)$, with $\gamma \equiv z_0 \omega_0^2$. By dynamical equivalence, the fluid motion satisfies an equation governing a layer in a tank at rest subjected to a time-dependent acceleration $-g + z_0 \omega_0^2 \cos(\omega_0 t)$. In the following, the function $z = \xi(x, y, t)$ quantifies the vertical displacement of the free surface with respect to rest, at time t and horizontal location (x, y).

The originality of this process with respect to the standard Faraday experiment is the presence of the drop acting as a periodic generator of perturbations on the surface. The droplet dynamics itself depends on the surface dynamics through the impacts. This system can be viewed as a nonlinear coupling between two sub-systems: an extended dynamical system (the liquid layer) sustaining waves and a 'particle' governed by an ordinary differential equation (ODE). This coupling changes the dynamics of both sub-systems. It is possible to distinguish two stages during the time evolution of the complete phenomenon: a first stage when the drop is almost in contact with the surface and exerts a pressure force that deflects the liquid; a second stage when the drop, being away from the surface, is in free fall and the surface of the liquid is decoupled from it. It is clear that during the first stage, highly nonlinear interactions take place. Even in the steady setting of a bath at rest, the bouncing of a drop is complex (Gopinath & Koch 2001, 2002; Bach, Koch & Gopinath 2004). It necessitates massive direct numerical simulations for two reasons: a large range of spatial scales (millimetre drop and micron-sized air film thickness $h_{film}(t)$ separating drop and liquid layer) and a large range of time scales (pressure increase below the drop is quite sudden and evolving as $h_{film}^{-3}(t)$). For the present unsteady case, the simultaneous drop and surface deformations lead to an even more involved problem. However, one

could further assume that the drop vertical motion is decoupled from the surface wave dynamics since the experimental ratio between surface deflection and maximum tank displacement z_0 is always less than 0.25. In this approximation, the surface is flat at each impact, which simplifies the problem but a global restitution coefficient for the drop must still be computed. This latter quantity is now dependent on two variables: the relative drop velocity and the phase of the tank acceleration at the moment of impact. This function is not presently available and it would require a huge numerical effort. A model based on a lubrication approximation exists (Vandewalle *et al.* 2008) but it assumes that the liquid layer surface does not deform. In this experiment, a non-negligible part of the drop energy loss is here contained in the wave generation by impact. Almost certainly, the dependence of the restitution coefficient on the phase is important to obtaining the lock-in behaviour between drop and wave in the walker experiment: indeed, the vertical motion of the drop is always periodic with double the forcing period. The system thus seems robust and away from the chaotic behaviour. *A contrario*, a model where a coefficient of restitution is phase dependent, produces a vertical chaotic behaviour within the range of experimental tank accelerations. Such a chaotic regime is experimentally observed for other parameters (drop sizes, oil viscosity or forcing frequency) but the walker dynamics is not present in such instances (Protière *et al.* 2006). Recently (Gilet & Bush 2009*a*, *b*), this chaotic bouncing has also been studied when the drop bounces over a soap film (in that instance the drop deformation is not considered). Another extreme model corresponds to a completely inelastic shock: the drop is in free fall away from the surface and when on the 'surface', it waits until the relative acceleration $-g + \gamma \cos(\omega_0 t)$ becomes positive. In that case, the times for impact and rebound can be precisely computed as a function of tank accelerations. This model, which has been studied by Pieranski (1983), produces a periodic, subharmonic and robust complete period doubling as observed experimentally. This model is satisfying in many aspects except that the complete rebound arises at acceleration $4.8\,g$ instead of the experimental observation $\gamma = 4.1\,g$. This discussion explains why it is almost impossible to get, based on an analysis of the physics, the whole coupled systems before a precise study of the bouncing is attempted. We prefer here to focus on the wave pattern and introduce the drop impact, i.e. the first stage, in a crude way using some hints from experimental observations. However, we demonstrate below that this method is sufficient to get the physical patterns observed in experiments.

6.1. *A single impact: the fluid mechanical model*

Below the Faraday instability threshold, the evolution of a single bump is the necessary ingredient to describe the more complex pattern produced by the walker. This specific pattern is obtained by computing the time evolution of a single impact located at the origin of space and at time t_{init}. This single event can also be compared with the experiment in which a ball is hitting the surface of the oscillating liquid, thus creating a unique perturbation.

An axisymmetric localized perturbation $\xi_{Bump}(r)$, with $r^2 = x^2 + y^2$ centred at the impact location, represents for the liquid layer the outcome of the first stage. It is chosen such that

$$\xi_{Bump}(r) = A_{pert}\left[-\exp\left(-\frac{r^2}{A_1^2}\right) + \frac{A_1^2 r^2}{A_2^4}\exp\left(-\frac{r^2}{A_2^2}\right)\right]. \qquad (6.1)$$

This ansatz represents a bump on the free surface with the average fluid elevation equal to zero. It corresponds to a structure similar to that expected after impact and

from experimental observations: a hollow surrounded by a ring protruding above the surface at rest. The three parameters A_{pert}, A_1 and A_2 are assumed to scale with the drop radius R_{drop}. We set $A_{pert} = R_{drop}$, $A_1 = \beta_1 R_{drop}$ and $A_2 = \beta_2 R_{drop}$ with $\beta_1 = 1.7$, $\beta_2 = 2.4$. With the above values, the radius of curvature at $r = 0$ is twice the drop radius R_{drop}, as imposed in Gopinath & Koch (2001) to comply with the continuity of pressure. Actually, up to a scaling factor, the global amplitude A_{pert} plays no role in our model because of the assumed superposition principle (see below). Moreover, the precise shape produced by the drop, i.e. the precise coefficients β_1, β_2, does not modify the qualitative dynamics.

During the second stage, the surface evolves freely. Since we are studying a Faraday instability below threshold, it is reasonable to assume that the surface wave is well described by the linear theory. The solution $\xi(x, y, t)$ is found as in Benjamin & Ursell (1954) and Drazin & Reid (1981), the surface boundary conditions are linearized and the flow in the liquid layer is assumed irrotational. Since at $t = t_{init}$ the perturbation is axisymmetric $\xi(x, y, t_{init}) = \xi_{Bump}(r)$, it retains this characteristic because the tank boundaries are supposed far away. For pure numerical reasons (necessity to use discrete transforms, see below), we impose a radial cutoff r_c: the function $\xi(x, y, t)$ is assumed to be localized in a finite interval $r \in [0, r_c]$. Since the physical structures that are obtained are localized, the presence of such a cutoff does not change these solutions if the numerical domain is large enough. In that case, the general solution (see (4.87) in Drazin & Reid 1981) reads as

$$\xi(r, t) = \sum_{m=1}^{\infty} a_m(t) S_m(r) \quad \text{with} \quad \Delta S_m(r) + k_m^2 S_m(r) = 0, \tag{6.2}$$

where $a_m(t)$ satisfies an ODE (see below) and $S_m(r)$ is a complete set of orthogonal axisymmetric eigenfunctions of the two-dimensional Laplace operator with eigenvalues k_m. This implies that $S_m(r)$ are related to the standard Bessel functions $J_0(r)$. The radial cutoff imposes that function $S_m(r)$ vanishes at $r = r_c$. This leads naturally to the Hankel transform expansion

$$\xi(r, t) = \sum_{m=1}^{\infty} a_m(t) J_0\left(\frac{\alpha_m}{r_c} r\right), \tag{6.3}$$

where α_m, $m = 1, \ldots, \infty$ are the zeros of the Bessel function $J_0(x)$. Note that $k_m = \alpha_m / r_c$. By introducing expansion (6.3) into the linearized hydrodynamic problem, one reduces the partial differential problem to a finite system of Mathieu equations that govern the dynamics of coefficient $a_m(t)$:

$$\frac{d^2 a_m}{dt^2} + (\omega^2(k_m) - k_m \tanh(k_m h_0) \gamma \cos(\omega_0 t)) a_m = 0, \tag{6.4}$$

where pulsation $\omega(k)$ satisfies (2.1). We modify the above system by introducing a phenomenological term that accounts for the damping due to viscosity

$$\frac{d^2 a_m}{dt^2} + 2\nu_{phen} k_m^2 \frac{da_m}{dt} + (\omega^2(k_m) - k_m \tanh(k_m h_0) \gamma \cos(\omega_0 t)) a_m = 0. \tag{6.5}$$

The second term that contains the kinematic phenomenological viscosity ν_{phen} (in $\text{m}^2\,\text{s}^{-1}$) is necessary to get a threshold for Faraday instability and to operate close to but below the instability region. This form of the damping term mimics the internal dissipation from the Navier–Stokes equation in this ODE. Though simple, this approach provides a sufficient description for modes and threshold (see Kumar &

Tuckerman 1994 for a critical analysis). Finally, the initial conditions are given by the coefficients $a_m(t_{init})$ evaluated by a discrete Hankel transform of function (6.1). Similarly, an inverse Hankel transform gets back the surface at time t from the coefficients $a_m(t)$.

In the numerical simulations, the parameter values corresponding to the experiment are $h_0 = 4$ mm for thickness of the liquid layer, $\sigma = 0.0209$ N m^{-1} and $\rho = 965$ kg m^{-3} for surface tension and density of silicon oil, $\omega_0 = 2\pi\ 80$ rad s^{-1} for the forcing frequency. From now on, all quantities are non-dimensionalized using the following two characteristic scales: time ω_0^{-1} and wavelength $\lambda_F = 2\pi/k_F$ (calculated so that $\omega(k_F)/\omega_0 = 1/2$, which gives $\lambda_F = 4.755$ mm). We thus have $T_F = 4\pi$. All quantities written in capital letters are assumed dimensionless. The function now reads as

$$\Xi(R, T) = \sum_{m=1}^{\infty} A_m(T) J_0(\alpha_m R/R_c) \qquad (6.6)$$

and the Mathieu equation becomes

$$\frac{d^2 A_m}{dT^2} + 2MK_m^2 \frac{dA_m}{dT} + (\Omega^2(K_m) - K_m \tanh(K_m H_0) Z_0 \cos T) A_m = 0, \qquad (6.7)$$

with

$$\Omega^2(K_m) = K_m G \tanh(K_m H_0)\{1 + \Lambda_{cap}^2 K_m^2\}, \qquad K_m = \frac{\alpha_m}{R_c}, \qquad (6.8)$$

$$\Lambda_{cap} = \sqrt{\sigma/(\rho g)}/\lambda_F, \quad G = g/(\lambda_F \omega_0^2), \quad Z_0 = z_0/\lambda_F, \quad M = \nu_{phen}/(\omega_0 \lambda_F^2). \qquad (6.9)$$

Note that $G = g/(\lambda_F \omega_0^2) = 8.18 \times 10^{-3}$ and the capillary length $2\pi\sqrt{\sigma/(\rho g)}$ is twice the Faraday length, since $\Lambda_{cap} = 0.31$. For numerical simulations, we truncate (6.6) to N terms

$$\Xi(R, T) = \sum_{m=1}^{N} A_m(T) J_0(\alpha_m R/R_c) \qquad (6.10)$$

and solve the Mathieu equations governing the first N modes. Typically, we have chosen $N = 800$–1000 with a cutoff radius $R_c = 20$–30. If the cutoff R_c is larger, we need a large enough N to ensure that the expansion (6.10) with N coefficients $A_m(T)$ fairly well approximates function (6.1). The coefficients $A_m(T)$ and the surface $\Xi(R, T)$ are obtained via a discrete direct or inverse Hankel transform from the GNU scientific library 1.8 (Galassi *et al.* 2009).

In order to get the value of M or, equivalently, the value of ν_{phen}, the Faraday instability threshold, which depends on the dissipative parameter, is computed. For the experimental forcing frequency $\omega_0 = 80$ Hz, the instability threshold is evaluated for the various wavenumbers $K_m = \alpha_m/R_c$ with respect to the relative acceleration Z_0/G: the dynamics of each amplitude $A_m(T)$ is computed at large times in order to determine if mode K_m exponentially increases or decreases. In figure 8, the curve giving the forcing threshold $(Z_0/G)_F$ is shown as a function of wavenumber K_m. Different curves correspond to different dimensionless viscosities M. As expected, the most unstable mode tends towards the Faraday wavenumber $K_F = 2\pi$ for vanishing viscosities. Experimentally, with silicon oil of viscosity $\mu = 20 \times 10^{-3}$ Pa s, the observed threshold is $(Z_0/G)_F = 4.1$. Comparing the thresholds with the experimental values, the dimensionless value $M = 2.7 \times 10^{-3}$ is chosen. If we were to assume that all dissipation is a bulk dissipation, i.e. can be modelled by a factor $2\nu k_m^2$ with ν being the true kinematic viscosity of silicon oil, one would obtain the crude approximation
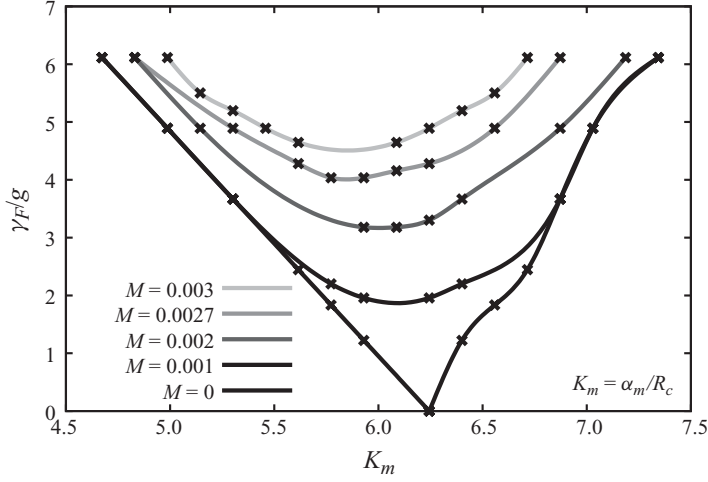
FIGURE 8. Instability threshold $(Z_0/G)_F = \gamma_F/g$ as a function of the mode wavenumber K_m in the case of a forcing frequency of $80\,\mathrm{Hz}$ for various values of dimensionless viscosity M.

$M = 1.76 \times 10^{-3}$. Since there exist other origins for the dissipation (e.g. boundary layers), the identified value is reasonable.

Below the Faraday instability threshold and in its vicinity, in the case of a supercritical problem, it is justified to use the linear theory, i.e. the Mathieu equation of the principal mode K_F (the less damped one, see (6.7)). First, let us change variables:

$$B(t) = A(t)\exp\left(-MK_F^2 t\right), \tag{6.11}$$

$$\frac{\mathrm{d}^2 B}{\mathrm{d}T^2} + \left(\Omega_1^2 - K_F \tanh(K_F H_0)Z_0 \cos T\right) B = 0, \tag{6.12}$$

with

$$\Omega_1^2(K_F) = \Omega_1^2(K_F) - M^2 K_F^4. \tag{6.13}$$

Near the instability threshold, we can use the asymptotic technique presented in Bender & Orszag (1978, pp. 560–566) to compute an asymptotic value for instance (11.4.15) in Bender & Orszag (1978). This gives the dominant term of $B(t)$, hence $A(t)$, which is written in dimensional variables as

$$A(t) \sim \exp\left(\left(\epsilon \omega_F - \nu k_F^2\right)t\right), \qquad \epsilon \equiv \tanh(kh_0)kz_0/2, \tag{6.14}$$

if we denote $\epsilon_c = \nu k_F^2/\omega_F$,

$$A(t) \sim \exp((\epsilon - \epsilon_c)\omega_F t). \tag{6.15}$$

This imposes that

$$\tau/T_F = 1/(2\pi(\epsilon - \epsilon_c)). \tag{6.16}$$

Hence, we recover the classical prediction used in §5:

$$\tau/T_F \propto \left(\frac{\gamma_F - \gamma}{\gamma_F}\right)^{-1}. \tag{6.17}$$

6.2. *A single impact: spatio-temporal evolution*

In figure 9, the evolution $\Xi(R, T)/A_{pert}$ of a single bump generated at time $T = 0$ is displayed for time $0 < T < 3.5$ and for two different radii R_{drop}. Two structures can be observed: a front that moves out from the point where the bump is created and a
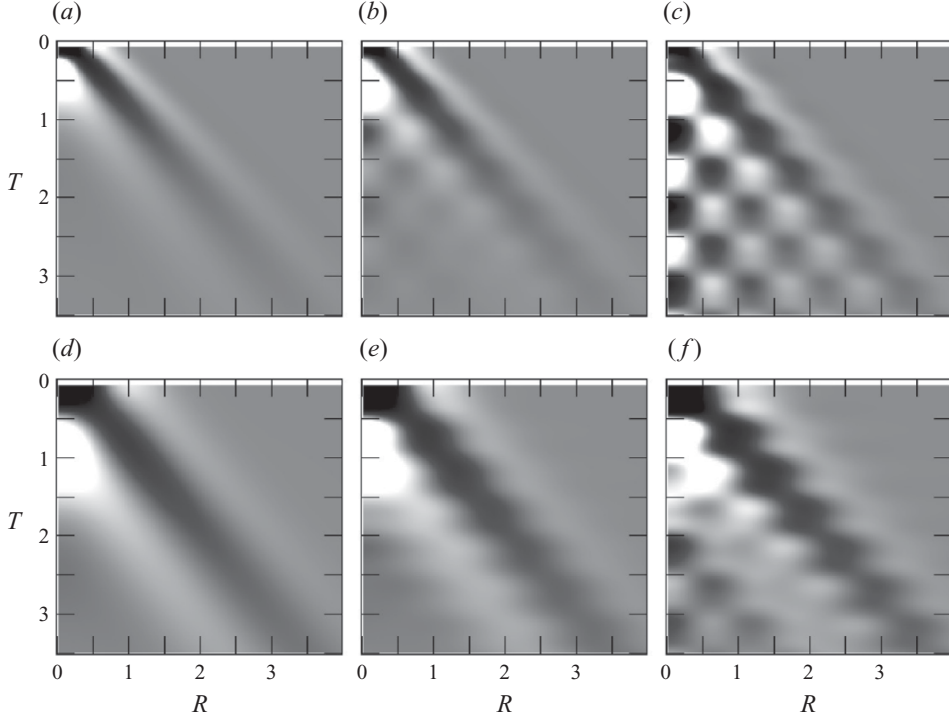
FIGURE 9. Evolution $\Xi(R,T)/A_{pert}$ for time $0 < T < 3.5$ of a single bump generated at time $T = 0$ with a forcing amplitude $Z_0/G = 0$ ($Me = 0$) (a,d), $Z_0/G = 1.52$ ($\Gamma^{-1} = 0.6$) (b,e), or $Z_0/G = 4.05$ ($\Gamma^{-1} = 82$) (c,f). Plots (a–c) are obtained with the droplet size $R_{drop} = 0.5$ mm, which corresponds to the experimental situation. Plots (d–f) are obtained with a larger droplet $R_{drop} = 1$ mm. The forcing frequency is fixed at 80 Hz. The dimensionless dissipation is set to $M = 2.7 \times 10^{-3}$ to ensure that the instability threshold is located at $(Z_0/G)_F = 4.1$.

standing wave pattern that spreads behind the front. Without forcing (see figure 9a,d), only the propagating front is present: this is the usual localized perturbation formed by a capillary front propagating outwards. The structure in the wavepacket depends on the wavelengths available in the initial bump $\xi_{Bump}(R)$. The velocity of the wavepacket is the group velocity. The main crest inside this wavepacket moves at the Faraday phase speed V_ϕ. In the presence of forcing (figure 9b,c,d,f), this propagating front is still present. However, when getting closer to the Faraday instability threshold ($Z_0/G = 1.52$ or 4.05), a second type of pattern emerges behind the capillary front. It is formed by damped standing Faraday modes. Wavenumbers close to the Faraday modes are initially present in the spectrum of the propagating wavefront and are the least damped afterwards. These structures survive while most of the other components of the spectrum rapidly decay, as experimentally observed (see figure 5).

Note that for a droplet's size similar to that used in the experiments ($R_{drop} = 0.5$ mm), the structure that emerges contains energy in the range of the Faraday wavelength, so that the standing Faraday modes are more intense. *A contrario*, when a bigger drop is used (figure 9d–f), the Faraday wavelength is still present but weaker with respect to the capillary part. This might explain why, when changing oil and forcing frequency, the range of sizes corresponding to a walker is modified. Indeed, the appropriate droplet size could correspond to the one capable of generating at each impact a maximum energy content for the resonant Faraday wavelength.
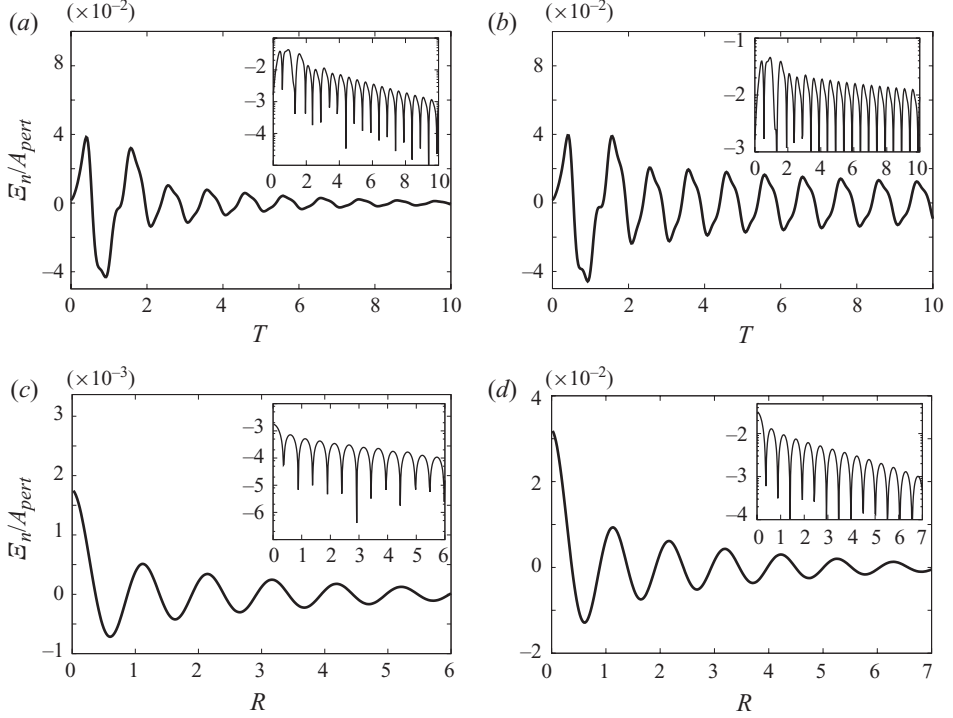
FIGURE 10. Numerical experiment with frequency $80\,\mathrm{Hz}$ and droplet size $R_{drop} = 0.5\,\mathrm{mm}$ (corresponding to the experimental situation). (*a*) Free surface height $\Xi_n(R, T)/A_{pert}$ at distance $R = 1$ from the impact point as a function of time (the impact occurred at $T = 0$). Forcing amplitude $Z_0/G = 3.3$ ($\Gamma^{-1} = 5.1$). Inset: height as a function of time T in semi-log scale. (*b*) Same as in (*a*) with $Z_0/G = 4.05$ ($\Gamma^{-1} = 82$). (*c*) Free surface height $\Xi_n(R, T)/A_{pert}$ at time $T = 11.475$ as a function of the distance R to the impact point. Forcing amplitude $Z_0/G = 3.3$ ($\Gamma^{-1} = 5.1$). Inset: height as a function of R in semi-log scale. The envelope can be fitted by the exponential function $2.27 \times 10^{-2} \exp(-0.305T)$. (*d*) Same as (*c*) with $Z_0/G = 4.05$ ($\Gamma^{-1} = 82$). The envelope can be fitted by the exponential function $7.9 \times 10^{-3} \exp(-0.019T)$.

As in experiments, the surface amplitude at a fixed position is observed to decrease in time (see figure 10*a,b*). In the insets, the semi-log scale indicates an exponential decay with a characteristic time $\tau/T_F = 3.28$ (figure 10*a*) or $\tau/T_F = 52$ (figure 10*b*). Here τ increases when getting closer to Faraday instability onset. Figure 10(*c,d*) presents, at a fixed time, the standing Faraday pattern. It decreases radially and the insets show an exponential damping. This indicates that a sum of such Bessel modes constitutes the standing wave pattern rather than a single mode, since it would impose an algebraic radial decay. This spatial damping is also confirmed in experiments.

6.3. *Steady bouncing drop*

As shown in §3, the walkers appear on the bath when the complete period doubling is achieved. Our aim in this section is to understand the role of this period doubling in the walking bifurcation. Here, we look at the nature of the wave field generated by a steady bouncing droplet in the framework of our fluid mechanics model. Note that, in this section, the droplet is constrained to be in a regime of steady bouncing without allowing for its propagation.

The drop impacts on the bath at specific times t_n, the index n discriminating between separate impacts. We choose the spatial origin at the impact location. Since
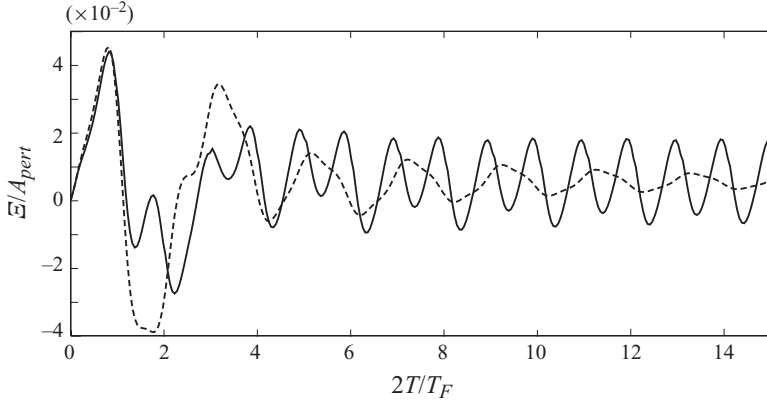
FIGURE 11. Time evolution of the surface height $\Xi(R, T)/A_{pert}$ at a distance $R = 1$ from the impact point. Forcing frequency 80 Hz, forcing amplitude $Z_0/G = 3.3$ ($\Gamma^{-1} = 5.1$), viscosity $M = 2.7 \times 10^{-3}$ and phase $\phi = 0$. The dashed line corresponds to a single drop impact and bold line corresponds to a steady bouncing at forcing frequency.

we assumed the linear theory to be valid for Faraday instability below threshold, the superposition principle holds and the general solution for the wave field reads as

$$\xi(x, y, t) = \sum_n \xi_n(x, y, t). \tag{6.18}$$

The effect of a drop impact at time t_n is identical to the single impact described above (§ 6.2) shifted in time at $t - t_n$. We have

$$\xi_n(x, y, t) = \xi(x, y, t - t_n). \tag{6.19}$$

This wave $\xi_n(x, y, t)$ evolves freely for $t > t_n$. We re-write this equation with non-dimensional quantities:

$$\Xi(R, T) = \sum_n \Xi_n(R, T) \quad \text{with} \quad R^2 = X^2 + Y^2. \tag{6.20}$$

First, we focus on the case of steady bouncing at the forcing frequency. We have $T_n = 2\pi n + \Phi$ in the sum (6.20), where Φ is the phase shift between the drop impact and the bath oscillation. The results found were similar for different values of Φ. In the steady state, the shape of the simulated pattern does not indicate the presence of a standing wave. The wave amplitude generated by the steady bouncing is smaller than that created by a single impact (see figure 11). This is also observed in the experimental case: the superposition of two consecutive impacts $\Xi_n(R, T)$ and $\Xi_{n+1}(R, T)$ is destructive as they are out of phase for Faraday instability.

In the case of bouncing at the Faraday frequency f_F, the drop impacts every two periods of vibration, i.e. $T_n = 4\pi n + \Phi$, in the sum (6.20). The interferences between $\Xi_n(R, T)$ and $\Xi_{n+1}(R, T)$ are in phase with the Faraday instability and consequently become additive. The amplitude generated by this bouncing at half the forcing frequency is larger than that of a single impact (see figure 12*a,b*). The pattern appears and reaches a steady state after several bouncing periods. As we get nearer to the threshold, this transient lasts longer. For instance, in figure 12(*a*), the saturation occurs after 15 bounces ($Z_0/G = 3.7$), while in figure 12(*b*) ($Z_0/G = 4.05$), it occurs after more than 50 bounces. After this transient, one readily observes a standing wave pattern with the Faraday frequency (see figure 12*c*). In addition, the amplitude in the steady
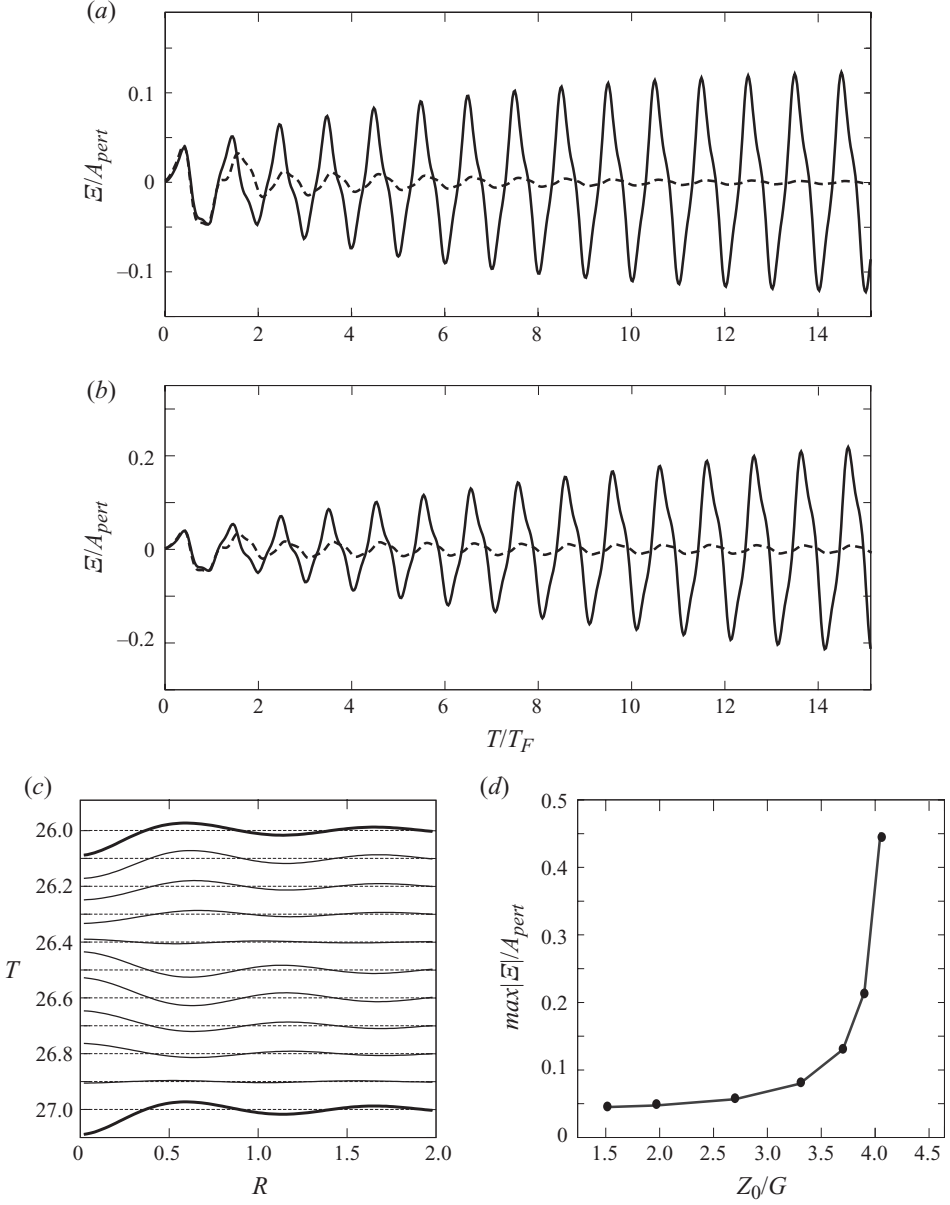
FIGURE 12. (a) Time evolution of the surface height $\Xi(R, T)/A_{pert}$ at a distance $R = 1$ from the impact point as a function of time. Forcing frequency 80 Hz, forcing amplitude $Z_0/G = 3.7$ ($\Gamma^{-1} = 10.2$), viscosity $M = 2.7 \times 10^{-3}$ and phase $\phi = 0$. Dashed line corresponds to a single drop impact and bold line corresponds to a steady bouncing at the Faraday frequency. (b) Similar to (a), but with $Z_0/G = 4.05$ ($\Gamma^{-1} = 82$). (c) Time evolution $\Xi(R, T)/A_{pert}$ of a steady bouncing at the Faraday frequency. Forcing frequency 80 Hz and forcing amplitude $Z_0/G = 4.05$ ($\Gamma^{-1} = 5.1$), for different times T, $M = 2.7 \times 10^{-3}$. The amplitude vertical scale has been rescaled to be easily seen. The thick curve corresponds to the time of impact. (d) Amplitude in the steady state at point $R = 1$ as a function of the forcing amplitude $Z_0/G = z_0\omega_0^2/g$. Forcing frequency 80 Hz, viscosity $M = 2.7 \times 10^{-3}$ and $\phi = 0$.
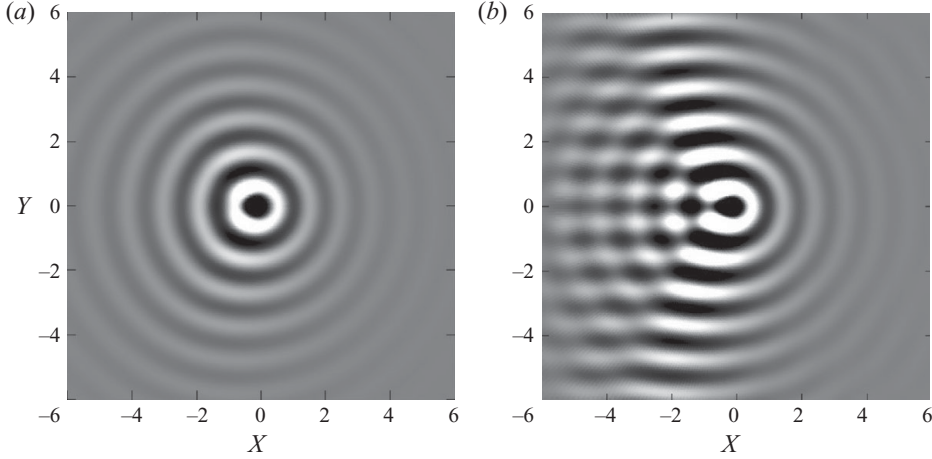
FIGURE 13. The surface height $\Xi(X, Y, T)$ of a walking droplet. (a) Forcing amplitude $Z_0/G = 3.7$ ($\Gamma^{-1} = 10.2$), velocity $V_W/V_\phi = 5.0 \times 10^{-2}$. (b) Forcing amplitude $Z_0/G = 4.05$ ($\Gamma^{-1} = 82$), velocity $V_W/V_\phi = 6.3 \times 10^{-2}$. For both plots the forcing frequency is set to 80 Hz and the dimensionless viscosity $M = 2.7 \times 10^{-3}$.

state increases when we get closer to the onset (see figure 12d). Actually, the characteristic damping time is larger when $\Gamma \ll 1$, and the number of contributive impacts increases accordingly. This behaviour is similar for various Φ and, quantitatively, it can be modified at most by a factor three. This increase of the wave amplitude with the forcing acceleration is the signature of the memory effect.

6.4. *Moving bouncing drop*

In the experiments, the bouncing at half-frequency is associated with motion. In this section, we compute the wave field $\xi_W(x, y, t)$ of a walker by adding single impacts with a moving source. We need to shift them both in time and space: the droplet bounces on the surface each Faraday period and moves with constant velocity V_W. We assume that the droplet is moving along the x-axis. The source points, indexed by n, are separated by a spatial distance $\Delta = \lambda_F V_W/V_\phi$ (with $\Delta \ll \lambda_F$ as $V_W \ll V_\phi$). By a trivial choice of space–time origin, the walker is supposed to impact at times $t_n = n/f_F$ at $x_n = n\Delta$. For $t_i < t < t_{i+1}$:

$$\xi_W(x, y, t) = \sum_{n=-\infty}^{i} \xi(x - x_n, y, t - t_n). \tag{6.21}$$

We re-write this equation using non-dimensional quantities:

$$\Xi_W(X, Y, T) = \sum_{n=-\infty}^{i} \Xi(X - X_n, Y, T - T_n). \tag{6.22}$$

Figure 13 presents the results of these computations. Far from the Faraday onset and with a slow walker, the wave field is approximately circular, with small variations of the wavelength (see figure 13a). Closer to the onset, a walker with a higher velocity creates a wave field similar to the Fresnel pattern (see figure 13b). This confirms both experimental observations and results obtained by the phenomenological model.
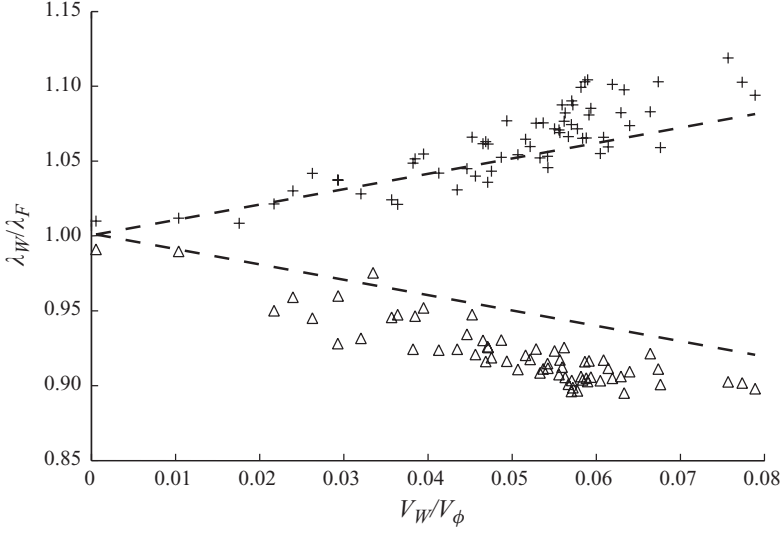
FIGURE 14. Measurement of the non-dimensional wavelength λ_W/λ_F as a function of the dimensional velocity V_W/V_ϕ of the walker for various droplets. The triangles show the wavelength ahead of the droplet, the crosses behind it. The dashed lines are the Doppler shift values given by (7.2).

7. The walker's wave field

We can now describe the walker's wave field in detail. Both the experimental results (§ 5) and the fluid mechanics theoretical approach (§ 6) have clarified the physics of a single impact on a vibrating bath. They demonstrated the need to distinguish two successive phases in the generation of waves by a bounce of the droplet. First, a capillary wavepacket is emitted and radiated away. This propagative front is centred on the bouncing point and travels at the group velocity V_g, while its main crest propagates with the phase speed V_ϕ. As it is radiated away, this front leaves behind a pattern of circular standing Faraday waves, which are almost sustained by the vertical forcing. Their damping time depends on the distance to γ_F, and they are long lasting when the system is tuned close to the instability onset. The global wave field results from the superposition of the recently emitted propagative front with the interference pattern of the synchronized standing Faraday waves generated by earlier bounces. First, we focus on the propagative fronts, then we examine the standing waves, and finally contributions of both effects are combined.

7.1. *The propagating fronts: Doppler effect*

If measurements are performed on the photographs shown in figure 2, they reveal that the succession of the main wave crests does not have the same spatial periodicity in all directions. Transverse to the motion, the pattern has exactly the wavelength expected for waves excited at half the forcing frequency. Ahead of the droplet, the waves appear compressed while they are dilated behind it. We measured the wavelengths λ_W along the direction of propagation, ahead of and behind the droplet, as a function of the walker's velocity V_W. These experimental results are presented in figure 14. They correspond to a Doppler shift. Observation of the high-speed camera films shows that in the vicinity of the bouncing droplet, the successive wave crests can be ascribed to the successive propagative wave fronts of the latest bounces. These wave crests travel with a phase speed V_ϕ and are generated by a source, the walker, that moves with

a constant speed V_W along the x-axis. We look at the wave pattern at time $t_0 = 0$, where the walker is located at $x_0 = 0$. Each crest is centred on a given impact point $x_n = n\Delta$ $(n < 0)$ and has travelled during $t_i - t_n$ a distance $|n\lambda_F|$. The wave maxima (x_{max}, y_{max}) are thus located on circles:

$$(x_{max} - x_n)^2 + y_{max}^2 = (n\lambda_F)^2, \tag{7.1}$$

with n being an integer. From (7.1), we can calculate the wavelength ahead of and behind the droplet. The equation simplifies to

$$\lambda_W^{th} = \lambda_F \mp V_W T_F. \tag{7.2}$$

As seen in figure 14, this predicted Doppler effect (7.2) is slightly weaker than the measured one. The origin of this discrepancy is not known.

7.2. *The sustained wave field: a stored memory*

We now focus on the standing waves by a trick whereby the existence of a path memory, supported by a sustained wave pattern, appears clearly. On a clean liquid interface, the lifetime of a walker is unlimited. However, the droplet will coalesce with the bath instantly if it collides with a floating bubble. By generating micro-bubbles on the interface, we can create a 'minefield' for the walker and observe with a high-speed camera a close-up of its coalescence. Figure 15(a–d) presents four successive images extracted from such a recording, where each subfigure shows images taken before the coalescence of the drop, at the coalescence, and surviving waves at times $t = 5T_F$ and $t = 15T_F$ after coalescence, respectively. At first sight, the wave patterns observed before and after the walker's disintegration appear very similar but they are actually different.

In the presence of the droplet, the whole pattern moves with the particle at velocity V_W. At each step, the new impact generates a circular propagative front, which is responsible for the translation of the whole pattern.

(i) After the walker disintegration, the capillary waves are radiated away and only the Faraday waves remain. The wave field still exhibits a complex interference pattern but the whole structure no longer propagates. The Doppler effect has disappeared and the wavelength is now the same and equal to λ_F in all directions.

(ii) Through lack of the energy imput due to the drop bouncing, the localized mode of Faraday waves decays with a typical time scale τ.

We recover the same three features in numerical simulations: we use the same procedure as in §6.4, but we stop adding the sources at a given time and let the system evolve. The wave field becomes stationary and the wavelength changes ahead of and behind the droplet (see figure 16).

In the long memory limit, this wave field results from the superposition of standing waves surrounding sources distributed along the past trajectory. Since the droplet had a rectilinear motion, these sources are aligned along the half-line behind the point at which the droplet has disappeared. These discrete sources are close to each other $(\Delta \ll \lambda_F)$. The waves are synchronized by the bath vibration and have an amplitude declining with time. The number of sources which contribute to the wave field is characterized by the memory parameter Me.

When Me tends to infinity, the wave field structure (figure 15c,d) can be understood by an optical analogy. A classical application of Huygens–Fresnel theory of diffraction (Huygens 1690) is the computation of the near-field interference pattern of a monochromatic plane wave impinging on the edge of a wall (Born & Wolf 1959). Behind the wall, the wave field is computed by replacing the plane wave by virtual
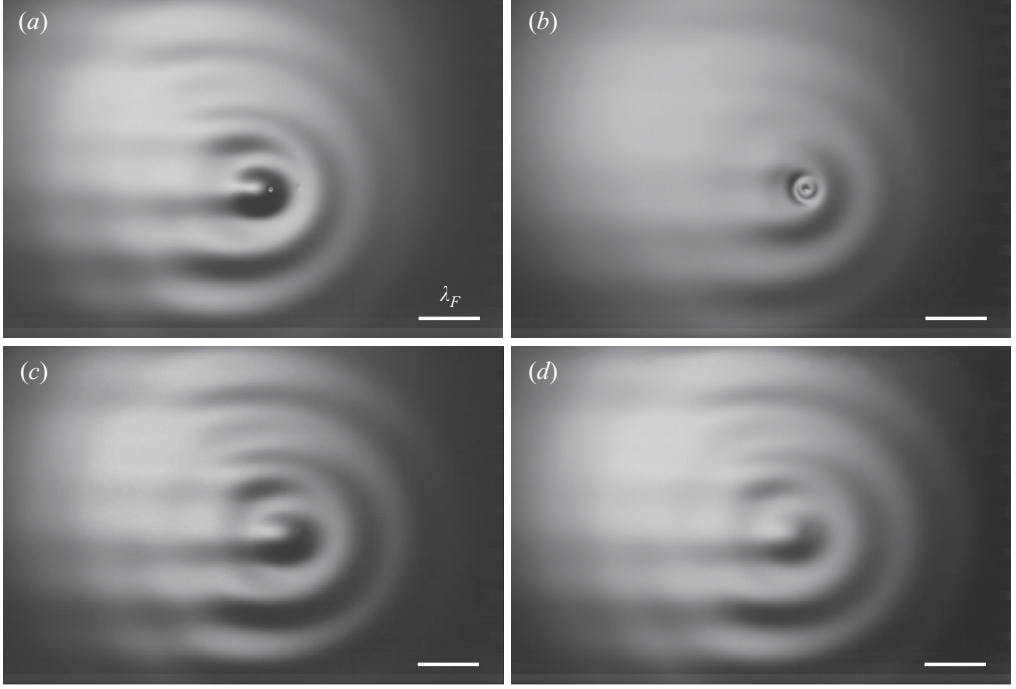
FIGURE 15. The disintegration of a walker. (a–d) Four photographs extracted from a fast camera film. If the origin of time is taken at the coalescence of the drop, the picture in (a) at time $t = -5T_F$ shows the wave field of the droplet that moves at velocity $V_W = 14.1\,\mathrm{mm\,s^{-1}}$ with $\Gamma^{-1} = 50$. In (b), the droplet collides with a small floating bubble and coalesces. The photographs in (c) and (d) taken at time $t = 5T_F$ and $t = 15T_F$ show the survival of standing waves, damping slowly with time. The white segments have a length equal to λ_F.
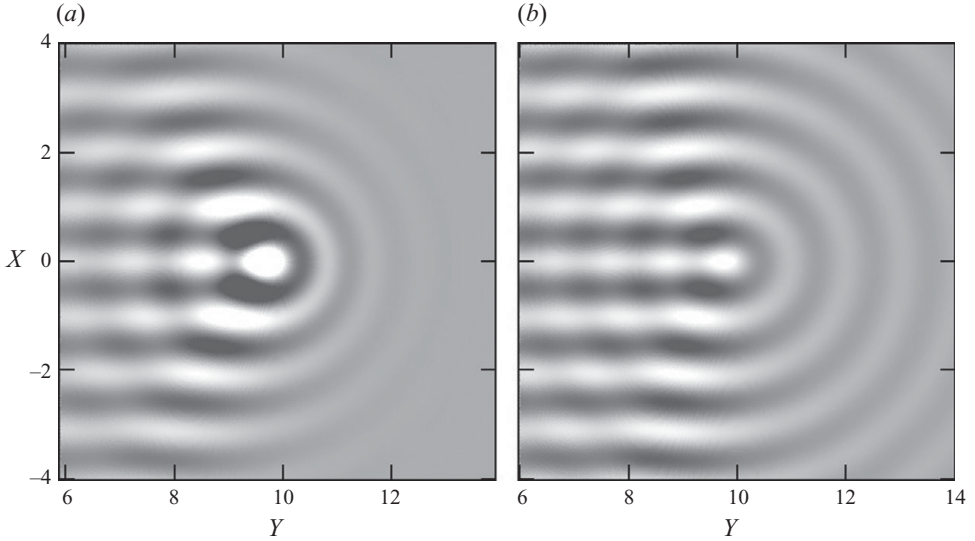

FIGURE 16. Two visualisations of $\Xi(X, Y, T)$ of a walker for a forcing frequency $80\,\mathrm{Hz}$ with a forcing amplitude $Z_0/g = 4.05$ ($\Gamma^{-1} = 82$), $M = 2.7 \times 10^{-3}$ and velocity $V_W = 0.2$. The drop has started to walk at time $T = 0$ and has disappeared at time $T = 42$. The wave field in (a) was obtained at $T = 41$ and in (b) at $T = 49$.

sources. These are in-phase sources of circular waves covering the unobstructed part of the wall plane. The sum of their contributions is then obtained by the geometrical construction of the Cornu spiral (Cornu 1874) or by the analytical calculation with the tabulated Fresnel integrals. In the vicinity of the edge, interference is observed while a plane wave is recovered far from it.

In our experiment, the previous points of bouncing are the centres of circular waves that are synchronized and aligned. Their geometrical distribution is the same as that of the virtual sources considered in optics, the equivalent of the wall being the half-line that has not yet been visited by the walker. The difference is of course that we have here real centres of standing waves instead of virtual sources of propagative waves. This analogy allows a precise description in the case of long path memory: after the drop destruction, the remaining memory field is a pure stationary Fresnel interference pattern that damps out very slowly. In the spatial vicinity of the last bounce of the drop, the nodes and antinodes are precisely predicted and a plane wave structure parallel to the trajectory is observed far from it. In the case of moderate path memory, the older sources generate waves of decreasing amplitude. In this case, the interference pattern near the last bounce is maintained. Far behind it, the plane wave part of the field vanishes.

7.3. *The global structure of the wave field*

Having presented separately the two components of a walker's wave field, we can return to its global description, taking into account the propagative fronts and the standing waves together. We can now revisit the three photographs shown in figure 2(*b*–*d*). They correspond to wave fields with a characteristic memory of 6, 14 and 55 bounces, respectively. In these photographs, the circular waves are mainly due to the successive capillary fronts emitted by the last few bounces and they exhibit a Doppler effect. These waves superpose on the stationary waves sustained around an increasingly large number of older collision sites (going from figures 2*b* to 2*d*). As already described, the interference of these Faraday waves produces standing plane waves parallel to the trajectory behind the droplet. They are particularly well observed in the situation of very weak damping ($Me \simeq 100$) in figure 17(*a*). The wave maxima (x_{max}, y_{max}) are located on lines $y_{max} = m \, \lambda_F$ parallel to the trajectory, m being an integer. The two types of waves being temporally synchronized by the forcing, their superposition gives rise to an interference pattern which is similar to the Fresnel interference pattern but includes a Doppler shift. Looking at the spatial phase of the waves, we can calculate the position of the maxima (x_{max}, y_{max}) of the wave field at the intersections of the two sets of curves:

$$\left. \begin{aligned} y_{max} &= m \, \lambda_F, \\ x_{max} &= n \, \Delta - \sqrt{(n^2 - m^2)} \, \lambda_F \quad \text{with } n < 0. \end{aligned} \right\} \tag{7.3}$$

All the extrema are placed along curves, drawn in figure 17(*b*). There is a good agreement with experimental observations in the case of weak damping. This simple model thus provides a good approximation of the wave structure.

8. Conclusion and outlook, the nature of the path memory

Several previous experiments on walkers have been dedicated to the question of how a localized and discrete particle could have a common dynamics with its extended associated wave. They revealed that, in spite of the huge gap between the systems, analogies exist with some aspects of the particle–wave behaviour at quantum scale.
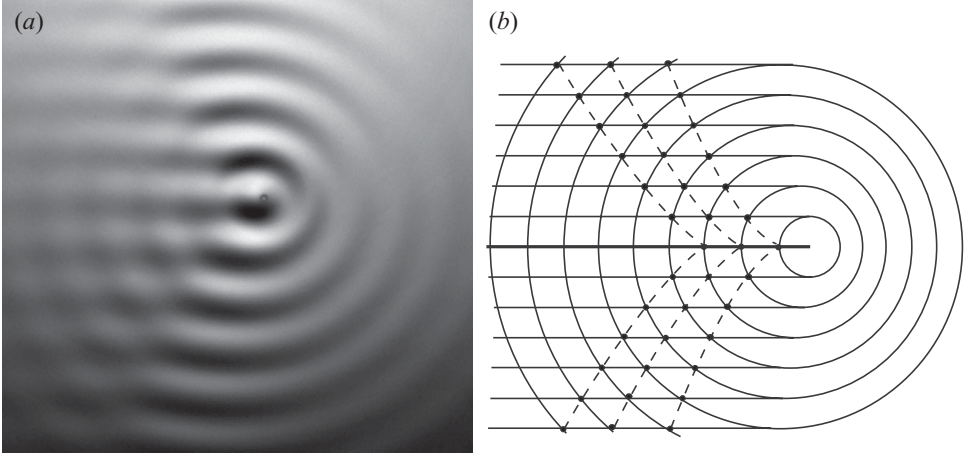
FIGURE 17. (*a*) Photograph of the wave field of a walker with $\Gamma^{-1} = 100$. (*b*) Sketch of the wave field. The circles are the antinodes of the capillary waves generated by the most recent impacts. The straight lines are the antinodes of the wave generated by the sources aligned with the past trajectory. The dotted lines are the resulting antinodal lines of the interference pattern.

For instance, the experiments on the diffraction of walkers (Couder & Fort 2006) showed that an attempt to localize the wave generates an uncertainty in the velocity of the droplet. A relation to quantum systems was also found in the quantization of the possible orbits when a walker is subjected to a force giving it a circular trajectory (Fort *et al.* 2010).

Early in the history of quantum mechanics, de Broglie suggested that elementary particles could be guided by their association with a pilot wave (de Broglie 1926). In an attempt to restore determinism in quantum mechanics, this idea was revisited by Bohm (1952). Our system, in which a particle (the droplet) is guided by its associated wave, appears as the first experimental implementation of the idea of a pilot wave and it does lead to quantum-like behaviours. However, in our system, while the association of the particle with the wave is a necessary condition to obtain those behaviours, it is not sufficient. Their observation also requires that the waves contain information on the droplet's past trajectory, what was called (Fort *et al.* 2010) the *wave-mediated path memory* of the system.

In many instances, the dynamics of physical systems depends on their history, for example when retardation effects exist. It is also a dominant feature of growth problems. For instance, in the case of a radially growing Saffman–Taylor viscous fingering, the structure of the initial destabilization continues contributing to the Laplacian field which determines the later growth (Couder 2000). Similarly, the high-order Fibonacci organization observed in the capitulum of a sunflower is the product of a sequence of successive bifurcations during the whole plant development (Douady & Couder 1996). In those cases, the system is open and changes with time.

The relation of a walker to its history is different. The system remains the same but its sensitivity to its own history is mediated by the existence of a recorded memory. This situation is met in biology or anthropology more often than in physics. In general terms, a memory requires the encoding of information, its storage and the possibility of a later access to this information. Here, each bounce of the droplet, by disturbing the interface, records information about the spatio-temporal localization

of the collision. This information is stored because each bounce generates a sustained localized state of Faraday waves. The information being stored in waves, the data about the trajectory are cumulated in an interference pattern due to the waves' linear superposition. Later, as the drop collides again with the interface, it 'reads' this cumulated information and the local slope of the distorted surface determines the direction and amplitude of the next jump. The dual nature of the walker is contained in the path memory dynamics: the wave nature lies in the coding while the particle nature lies in the reading. The reading can be seen as a local integration of the wavepacket at a single localized point. It can be noted that a related situation has been observed recently in crack propagations (Goldman, Livne & Fineberg 2010), where waves emitted in the past can return to act on the propagating crack at later times.

The present article has addressed the quantitative characterization of this path memory. We have first studied the excitation of Faraday waves by a single disturbance below the instability threshold. Turning to the case of a linear moving droplet, we have shown that its global wave field can be entirely described by the superposition of waves excited along a straight line by the successive impacts of its bouncing. We have thus shown that when a walker is far from any boundary, there exists a translating global solution for both the droplet and the interference pattern of the wave field.

However, the memory has very drastic effects when the trajectory is not rectilinear. When the walker is forced into a circular motion by an applied transverse force, only certain trajectories are possible, generating a wave field with a fixed structure that rotates with the droplet. This leads to a quantization of the possible orbits as shown in Fort *et al.* (2010). Other dramatic effects of the memory are observed whenever boundaries generate any kind of confinement of the walker. In these situations, the waves emitted in the past and reflected by the boundaries lead to a complex structure of the interference field and correspondingly to a disorder in the droplet motion (Couder & Fort 2006). The present quantitative analysis will be an essential tool for a further investigation of those situations where a forced spatial localization generates an uncertainty in the walker velocity. Finally, the possible relevance of this type of temporal non-locality to particle physics appears an interesting open problem.

REFERENCES

ARANSON, I. S., GORSHKOV, K. A., LOMOV, A. S. & RABINOVICH, M. I. 1990 Stable particle-like solutions of multidimensional nonlinear fields. *Physica* D **43**, 435–453.

BACH, G. A., KOCH, D. L. & GOPINATH, A. 2004 Coalescence and bouncing of small aerosol droplets. *J. Fluid Mech.* **518**, 157–185.

BENDER, C. M. & ORSZAG, S. A. 1978 *Advanced Mathematical Methods for Scientists and Engineers.* McGraw-Hill.

BENJAMIN, T. B. & URSELL, F. 1954 The stability of a plane free surface of a liquid in vertical periodic motion. *Proc. R. Soc. Lond.* A **225**, 505–515.

BOHM, D. 1952 A suggested interpretation of the quantum theory in terms of hidden variables. *Phys. Rev.* **85**, 166–179.

BORN, M. & WOLF, E. 1959 *Principles of Optics.* Cambridge University Press.

DE BROGLIE, L. 1926 *Ondes et mouvements.* Gautier Villars.

BURKE, J. & KNOBLOCH, E. 2006 Localized states in the generalized Swift–Hohenberg equation. *Phys. Rev.* E **73**, 056211.

CILIBERTO, S. & GOLLUB, J. P. 1984 Pattern competition leads to chaos. *Phys. Rev. Lett.* **52**, 922–925.

CORNU, A. 1874 Méthode nouvelle pour la discussion des problèmes de diffraction dans le cas d'une onde cylindrique. *J. Phys.* **3**, 44.

COUDER, Y. 2000 Viscous fingering as an archetype for growth patterns. In *Perspectives in Fluid Dynamics* (ed. G. K. Batchelor, H. K. Moffat & M. G. Worster), pp. 53–104. Cambridge University Press.

COUDER, Y. & FORT, E. 2006 Single particle diffraction and interferences at macroscopic scale. *Phys. Rev. Lett.* **97**, 154101.

COUDER Y., FORT, E., GAUTIER, C. H. & BOUDAOUD, A. 2005a From bouncing to floating: noncoalescence of drops on a fluid bath. *Phys. Rev. Lett.* **94**, 177801.

COUDER, Y., PROTIÈRE, S. FORT, E. & BOUDAOUD, A. 2005b Dynamical phenomena: walking and orbiting droplets. *Nature* **437**, 208.

DOUADY, S. 1990 Experimental study of the Faraday instability. *J. Fluid Mech.* **221**, 383–409.

DOUADY, S. & COUDER, Y. 1996 Phyllotaxis as a dynamical self-organizing process, the simulation of the transient regimes of ontogeny. *J. Theor. Biol.* **178**, 295–312.

DOUADY, S. & FAUVE, S. 1988 Pattern selection in Faraday instability. *Europhys. Lett.* **6**, 221–226.

DRAZIN, P. G. & REID, W. H. 1981 *Hydrodynamic Stability*. Cambridge University Press.

EDDI, A., FORT, E., MOISY, F. & COUDER, Y. 2009 Unpredictable tunneling of a classical wave–particle association. *Phys. Rev. Lett.* **102**, 240401.

EDWARDS, W. S. & FAUVE, S. 1994 Patterns and quasi-patterns in the Faraday experiment. *J. Fluid Mech.* **278**, 123–148.

FARADAY, M. 1831 On the forms and states of fluids on vibrating elastic surfaces. *Phil. Trans. R. Soc. Lond.* **52**, 299.

FAUVE, S. 1998 Pattern forming instabilities. In *Hydrodynamics and Nonlinear Instabilities* (ed. C. Godreche & P. Manneville), pp. 387–491. Cambridge University Press.

FORT, E., EDDI, A., BOUDAOUD, A., MOUKHTAR, J. & COUDER, Y. 2010 Path-memory induced quantization of classical orbits. *Proc. Natl Acad. Sci. USA* **107** (41), 17515–17520.

GALASSI, M., DAVIES, J., THEILER, J., GOUGH, B., JUNGMAN, G., ALKEN, P., BOOTH, M. & ROSSI, F. 2009 *GNU Scientific Library Reference Manual*, 3rd edn. Network Theory Ltd.

GILET, T. & BUSH, J. W. M. 2009a Chaotic bouncing of a droplet on a soap film. *Phys. Rev. Lett.* **102**, 014501.

GILET, T. & BUSH, J. W. M. 2009b The fluid trampoline: droplets bouncing on a soap film. *J. Fluid Mech.* **625**, 167–203.

GOLDMAN, T., LIVNE, A. & FINEBERG, J. 2010 Acquisition of inertia by a moving crack. *Phys. Rev. Lett.* **104**, 114301.

GOPINATH, A. & KOCH, D. L. 2001 Dynamics of droplet rebound from a weakly deformable gas–liquid interface. *Phys. Fluids* **13**, 3526.

GOPINATH, A. & KOCH, D. L. 2002 Collision and rebound of small droplets in an incompressible continuum gas. *J. Fluid Mech.* **454**, 145–201.

GUCKENHEIMER, J. & HOLMES, P. 1983 *Nonlinear Oscillations, Dynamical Systems and Bifurcations of Vector Fields*. Springer.

HUYGENS, C. 1690 *Traité de la lumière*. Van der Aa.

KEOLIAN, R., TURKEVICH, L. A., PUTTERMAN, J., RUDNICK, I. & RUDNICK, J. A. 1984 Subharmonic sequences in the Faraday experiment: departures from period doubling. *Phys. Rev. Lett.* **47**, 1133–1136.

KOLODNER, P., BENSIMON, D. & SURKO, C. M. 1988 Traveling-wave convection in an annulus. *Phys. Rev. Lett.* **60**, 1723–1726.

KUMAR, K. & TUCKERMAN, L. S. 1994 Parametric instability of the interface between two fluids. *J. Fluid Mech.* **279**, 49–68.

LIEHR, A. W., MOSKALENKO, A. S., ASTROV, YU., A. BODE, M. & PURWINS, H.-G. 2004 Rotating bound states of dissipative solitons in systems of reaction–diffusion type. *Eur. Phys. J.* B **37**, 199–204.

LIOUBASHEVSKI, O. & FINEBERG, J. 2001 Shock wave criterion for propagating solitary states in driven surface waves. *Phys. Rev.* E **63**, 035302.

MOISY, F., RABAUD, M. & SALSAC, K. 2009 A synthetic Schlieren method for the measurement of the topography of a liquid interface. *Exp. Fluids* **46**, 1021–1036.

PIERANSKI, P. 1983 Jumping particle model: period doubling cascade in an experimental system. *J. Phys. (Paris)* **44**, 573–578.

PROTIÈRE, S., BOUDAOUD, A. & COUDER, Y. 2006 Particle–wave association on a fluid interface. *J. Fluid Mech.* **554**, 85–108.

RAMAZZA, P. L., BENKLER, E., BORTOLOZZO, U., BOCCALETTI, S., DUCCI, S. & ARECCHI, F. T. 2002 Tailoring the profile and interactions of optical localized structures. *Phys. Rev.* E **65**, 066204.

THUAL, O. & FAUVE, S. 1988 Localized structures generated by subcritical instabilities. *J. Phys.* **49**, 1829–1833.

TSIMRING, L. S. & ARANSON, I. S. 1997 Localized and cellular patterns in a vibrated granular layer. *Phys. Rev. Lett.* **79**, 213–216.

UMBANHOWAR, P. B., MELO, F. & SWINNEY, H. L. 1996 Localized excitations in a vertically vibrated granular layer. *Nature* **382**, 793–796.

VANDEWALLE, N., TERWAGNE, D., MULLENERS, K., GILET, T. & DORBOLO, S. 2008 Dynamics of a bouncing droplet onto a vertically vibrated surface. *Phys. Rev. Lett.* **100**, 167802.